

**Supporting Information for:**  
**Formation of the aminoperoxyl radical in the  
atmospheric oxidation of ammonia**

Vili-Taneli Salo,<sup>†,‡</sup> Jing Chen,<sup>‡</sup> and Henrik G. Kjaergaard<sup>\*,‡</sup>

*†Department of Chemistry, Faculty of Science, University of Helsinki, Helsinki FI-00014,  
Finland*

*‡Department of Chemistry, University of Copenhagen, 2100 Copenhagen, Denmark*

E-mail: hgk@chem.ku.dk

# Table of Contents

<b>S1</b>	<b><math>\text{CH}_3 + \text{O}_2 \longrightarrow \text{CH}_3\text{O}_2</math> reaction</b>	<b>S8</b>
<b>S2</b>	<b>High-pressure limit thermal rate coefficient calculations with the canonical variational theory</b>	<b>S9</b>
S2.1	Gibbs energy surfaces of $\text{NH}_2 + \text{O}_2 \longrightarrow \text{NH}_2\text{O}_2$ and $\text{CH}_3 + \text{O}_2 \longrightarrow \text{CH}_3\text{O}_2$ reactions	S10
S2.1.1	Harmonic vibrational analysis along the reaction coordinate . . . . .	S10
S2.1.2	Hindered internal rotation of the N-O and C-O bonds . . . . .	S13
<b>S3</b>	<b>Details of the Master Equation simulations with MESMER</b>	<b>S18</b>
S3.1	RRKM simulations . . . . .	S18
S3.2	ILT simulations . . . . .	S20
S3.3	ME results . . . . .	S20
S3.4	Sensitivity tests . . . . .	S24
<b>S4</b>	<b>Calculated fraction of <math>\text{NH}_2\text{O}_2</math> as a function of altitude</b>	<b>S28</b>
<b>S5</b>	<b>Calculated fraction of <math>\text{NH}_2\text{O}_2</math> under different experimental conditions</b>	<b>S29</b>
<b>S6</b>	<b><math>\text{NH}_2 + \text{O}_2 \rightarrow \text{NH}_2\text{O}_2</math>, calculated using CASPT2 and CASPT2-IPEA</b>	<b>S30</b>
<b>S7</b>	<b>Comparison of ATcT database reaction enthalpies and calculated reaction enthalpies</b>	<b>S32</b>
<b>S8</b>	<b>NEVPT2 calculations: structural parameters, CAS orbitals, vibrational frequencies, and rotational constants</b>	<b>S33</b>
<b>S9</b>	<b>Geometries of the stationary points at various levels of theory</b>	<b>S54</b>
S9.1	$\omega\text{B97X-D3/aug-cc-pVTZ}$ . . . . .	S54
S9.2	$\text{B3LYP(D3BJ)/aug-cc-pVTZ}$ . . . . .	S56
S9.3	$\text{CASPT2/aug-cc-pVTZ}$ . . . . .	S58
S9.4	$\text{NEVPT2/aug-cc-pVTZ}$ . . . . .	S59



# List of Figures

S1	a) Minimum energy path of the $\text{CH}_3 + \text{O}_2 \longrightarrow \text{CH}_3\text{O}_2$ reaction as a function of the $\text{H}_3\text{C}-\text{O}_2$ distance. b) Corresponding Gibbs energy surface, at 298K and 1 atm. Gradient of the potential projected out and the C-O torsion treated as a hindered rotation. Electronic energies and thermodynamic corrections obtained at NEVPT2(13e,9o) level. . . . .	S9
S2	Non-redundant internal coordinates used in present work. . . . .	S11
S3	Torsional potential as a function of a) N-O distance in $\text{NH}_2\text{O}_2$ , and b) C-O distance in $\text{CH}_3\text{O}_2$ . . . . .	S14
S4	Definition of the reduced moment of inertia in the a) $\text{H}_2\text{N}-\text{O}_2$ supermolecule, and b) $\text{H}_3\text{C}-\text{O}_2$ supermolecule. $r_{\text{NH}_1}=r_{\text{NH}_2}$ and $r_{\text{CH}_1}=r_{\text{CH}_2}=r_{\text{CH}_3}$ due to $C_s$ -symmetrization. S14	S14
S5	Fourier fits of the torsional potentials at a) $\text{NH}_2\text{O}_2$ minimum, b) $\text{H}_2\text{N}-\text{O}_2$ transition state, c) $\text{CH}_3\text{O}_2$ minimum, and d) $\text{H}_3\text{C}-\text{O}_2$ transition state. . . . .	S15
S6	Arrhenius fits of the $k_\infty^{CVT}$ rate coefficients for a) $\text{NH}_2 + \text{O}_2 \longrightarrow \text{NH}_2\text{O}_2$ , and b) $\text{CH}_3 + \text{O}_2 \longrightarrow \text{CH}_3\text{O}_2$ . . . . .	S20
S7	Pressure dependence of the reaction rate coefficients, in the pressure range of $10^{-4}$ – $10^4$ bar, at temperatures of 300 K ( <b>black</b> ), 275 K ( <b>red</b> ), 250 K ( <b>blue</b> ), 225 K ( <b>orange</b> ), and 200 K ( <b>violet</b> ). a) $\text{NH}_2 + \text{O}_2 \longrightarrow \text{NH}_2\text{O}_2$ , b) $\text{CH}_3 + \text{O}_2 \longrightarrow \text{CH}_3\text{O}_2$ , c) $\text{NH}_2\text{O}_2 \longrightarrow \text{NH}_2 + \text{O}_2$ , d) $\text{CH}_3\text{O}_2 \longrightarrow \text{CH}_3 + \text{O}_2$ . Obtained with ILT/ME. . . .	S21
S8	Heat map of the $\text{NH}_2\text{O}_2$ equilibrium fractions (%) as a function of the reaction conditions. Note that the partial pressure of $\text{O}_2$ is held at constant 21% of the total pressure across all pressures, to be consistent with atmospheric conditions. Values obtained with the ILT/ME method. . . . .	S23
S9	Dependence of the bimolecular association reaction rate coefficient (at 300 K) on the average energy lost $\langle \Delta E \rangle_d$ in collisions with the $\text{N}_2$ bath: 300 ( <b>black</b> ), 250 ( <b>red</b> ), 200 ( <b>blue</b> ), 150 ( <b>orange</b> ), and 100 ( <b>violet</b> ), in units of $\text{cm}^{-1}$ . a) $\text{NH}_2 + \text{O}_2 \longrightarrow \text{NH}_2\text{O}_2$ , b) $\text{CH}_3 + \text{O}_2 \longrightarrow \text{CH}_3\text{O}_2$ . HPL = high-pressure limit. Obtained with the ILT/ME method. . . . .	S24

S10	Dependence of the bimolecular association reaction rate coefficient (at 300 K) on the value of the relative energy difference ( $E_{\text{rel}}$ ) between reactants and products. Original value ( <b>red</b> ), $E_{\text{rel}}$ increased by 0.5 kcal mol <sup>-1</sup> ( <b>black</b> ), $E_{\text{rel}}$ lowered by 0.5 kcal mol <sup>-1</sup> ( <b>blue</b> ). a) $\text{NH}_2 + \text{O}_2 \longrightarrow \text{NH}_2\text{O}_2$ , b) $\text{CH}_3 + \text{O}_2 \longrightarrow \text{CH}_3\text{O}_2$ . Obtained with the ILT/ME method. . . . .	S25
S11	Equilibrium fraction of $\text{NH}_2\text{O}_2$ as a function of pressure and relative energy difference ( $E_{\text{rel}}$ ) between $\text{NH}_2 + \text{O}_2$ and $\text{O}_2$ , at 300 K. Original value ( <b>red</b> ), $E_{\text{rel}}$ increased by 0.5 kcal mol <sup>-1</sup> ( <b>black</b> ), $E_{\text{rel}}$ lowered by 0.5 kcal mol <sup>-1</sup> ( <b>blue</b> ). a) $\text{NH}_2 + \text{O}_2 \longrightarrow \text{NH}_2\text{O}_2$ , b) $\text{CH}_3 + \text{O}_2 \longrightarrow \text{CH}_3\text{O}_2$ . Obtained with the ILT/ME method. . . . .	S26
S12	Association reaction curve of $\text{NH}_2 + \text{O}_2 \longrightarrow \text{NH}_2\text{O}_2$ , obtained using CASPT2(13e,11o)/aug-cc-pVTZ and CASPT2-IPEA//CASPT2 methods, using a range of IPEA-shift values. The CCSD(T)/CBS// $\omega$ B97X-D3/aug-cc-pVTZ relative energy is shown for comparison ( $\star$ ). The hollow points correspond to the highest energy point located around the assumed saddle point. . . . .	S31
S13	$\text{NH}_2$ ( $\text{C}_{2v}$ ), NEVPT2(7e,6o)/aug-cc-pVTZ, bond lengths in the units of Ångström. .	S33
S14	$\text{O}_2$ ( $\text{D}_{\infty h}$ ) $^3\Sigma_g^-$ , NEVPT2(12e,8o)/aug-cc-pVTZ, bond lengths in the units of Ångström.	S34
S15	$\text{H}_2\text{N}\cdots\text{O}_2$ complex, NEVPT2(13e,11o)/aug-cc-pVTZ, bond lengths in the units of Ångström. . . . .	S35
S16	$\text{H}_2\text{N}\cdots\text{O}_2$ PES saddle point, NEVPT2(13e,11o)/aug-cc-pVTZ, bond lengths in the units of Ångström. . . . .	S36
S17	$\text{H}_2\text{N}\cdots\text{O}_2$ CVT transition state structure, NEVPT2(13e,11o)/aug-cc-pVTZ, bond lengths in the units of Ångström. . . . .	S37
S18	$\text{NH}_2\text{O}_2$ , NEVPT2(13e,11o)/aug-cc-pVTZ, bond lengths in the units of Ångström. .	S38
S19	$\text{NH}_2\text{O}_2$ to $\text{HNOOH}$ isomerization transition state, NEVPT2(13e,11o)/aug-cc-pVTZ, bond lengths in the units of Ångström. . . . .	S39
S20	$\text{HNOOH}$ , NEVPT2(13e,11o)/aug-cc-pVTZ, bond lengths in the units of Ångström. .	S40
S21	$\text{HNO}\cdots\text{OH}$ transition state, NEVPT2(13e,11o)/aug-cc-pVTZ, bond lengths in the units of Ångström. . . . .	S41

S22	HNO $\cdots$ OH complex, NEVPT2(13e,11o)/aug-cc-pVTZ, bond lengths in the units of Ångström. . . . .	S42
S23	HONHO, NEVPT2(13e,11o)/aug-cc-pVTZ, bond lengths in the units of Ångström. . . . .	S43
S24	HO $\cdots$ H–NO transition state, NEVPT2(13e,11o)/aug-cc-pVTZ, bond lengths in the units of Ångström. . . . .	S44
S25	HNO ( $C_s$ ), NEVPT2(12e,9o)/aug-cc-pVTZ, bond lengths in the units of Ångström. . . . .	S45
S26	NO ( $C_{\infty v}$ ), NEVPT2(11e,8o)/aug-cc-pVTZ, bond lengths in the units of Ångström. . . . .	S46
S27	H <sub>2</sub> O ( $C_{2v}$ ), NEVPT2(8e,6o)/aug-cc-pVTZ, bond lengths in the units of Ångström. . . . .	S47
S28	OH ( $C_{\infty v}$ ), NEVPT2(7e,5o)/aug-cc-pVTZ, bond lengths in the units of Ångström. . . . .	S48
S29	NH <sub>2</sub> O ( $C_s$ ), NEVPT2(13e,10o)/aug-cc-pVTZ, bond lengths in the units of Ångström. . . . .	S49
S30	O( <sup>3</sup> P), NEVPT2(6e,4o)/aug-cc-pVTZ. . . . .	S50
S31	CH <sub>3</sub> ( $D_{3h}$ ), NEVPT2(7e,7o)/aug-cc-pVTZ, bond lengths in the units of Ångström. . . . .	S51
S32	H <sub>3</sub> C $\cdots$ O <sub>2</sub> CVT transition state structure, NEVPT2(13e,9o)/aug-cc-pVTZ, bond lengths in the units of Ångström. . . . .	S52
S33	CH <sub>3</sub> O <sub>2</sub> , NEVPT2(13e,9o)/aug-cc-pVTZ, bond lengths in the units of Ångström. . . . .	S53

# List of Tables

S1	Convergence of the torsional partition function at 298 K as a function of number of Fourier terms used for $V(\theta)$ . . . . .	S17
S2	MESMER results of $\text{NH}_2 + \text{O}_2 \xrightleftharpoons[k_r]{k_f} \text{NH}_2\text{O}_2$ and $\text{CH}_3 + \text{O}_2 \xrightleftharpoons[k_r]{k_f} \text{CH}_3\text{O}_2$ reactions, at 298 K and 1 atm. . . . .	S22
S3	Pressures and temperatures at various altitudes, calculated with the barometric formula, using two surface temperature scenarios. . . . .	S28
S4	Calculated equilibrium fraction of $\text{NH}_2\text{O}_2$ under different experimental reaction conditions. <sup>[a]</sup> . . . . .	S29
S5	Comparison of ATcT database reaction enthalpies and calculated reaction enthalpies (at NEVPT2), in units of $\text{kcal mol}^{-1}$ . . . . .	S32

## S1 $\text{CH}_3 + \text{O}_2 \longrightarrow \text{CH}_3\text{O}_2$ reaction

All NEVPT2 calculations concerning the  $\text{CH}_3\text{O}_2$  molecule and related supermolecules were done using a CAS(13e,9o) active space, which consists of all oxygen valence orbitals, as well as the C-O bonding and antibonding orbitals. The geometries and frequencies of the isolated  $\text{CH}_3$  and  $\text{O}_2$  molecules were calculated using full-valence active spaces, which were CAS(7e,7o) and CAS(12e,8o), respectively. The reaction potential for the  $\text{CH}_3 + \text{O}_2 \longrightarrow \text{CH}_3\text{O}_2$  was obtained similarly to the  $\text{NH}_2 + \text{O}_2 \longrightarrow \text{NH}_2\text{O}_2$  (discussed in the main article). First, the structure of the minimum,  $\text{CH}_3\text{O}_2$ , was optimized at the NEVPT2(13e,9o)/AVTZ level, after which the reaction potential was studied by carrying a relaxed scan of the C-O bond length, up to 3.0 Å distance, while relaxing all other degrees of freedom. The reaction potential is shown in Fig. S1. The reaction energies were estimated also with other methods, see the legend in Fig. S1a. The NEVPT2(13e,9o) energy of the non-interacting pair of  $\text{CH}_3$  and  $\text{O}_2$  (notated with the  $\infty$  symbol in the horizontal axis of Fig. S1a) was calculated by elongating the C-O distance to 30 Å and carrying out a relaxed optimization with respect to this distance constraint. Notably, all the used methods agree on the reaction energy within 2 kcal mol<sup>-1</sup>. Just like for the  $\text{NH}_2\text{O}_2$  system, we used the reaction energy obtained at the W3X-L level for further calculations.

Fig. S1b shows the corresponding quasi-thermodynamic (gradient of the potential projected at all points) Gibbs energy surface of the reaction, at 298K and 1atm. The Gibbs energy surface has a maximum at 2.43 Å C-O distance, and this structure was used as the transition state in CVT calculations. The C-O torsion is almost barrierless at this point (Fig. S5d), so we used a free rotor partition function instead of hindered rotor in the CVT calculations of the transition state. Furthermore, we verified that the location of the Gibbs energy maximum was not sensitive to whether a free rotor or hindered rotor model was used for the C-O torsion.

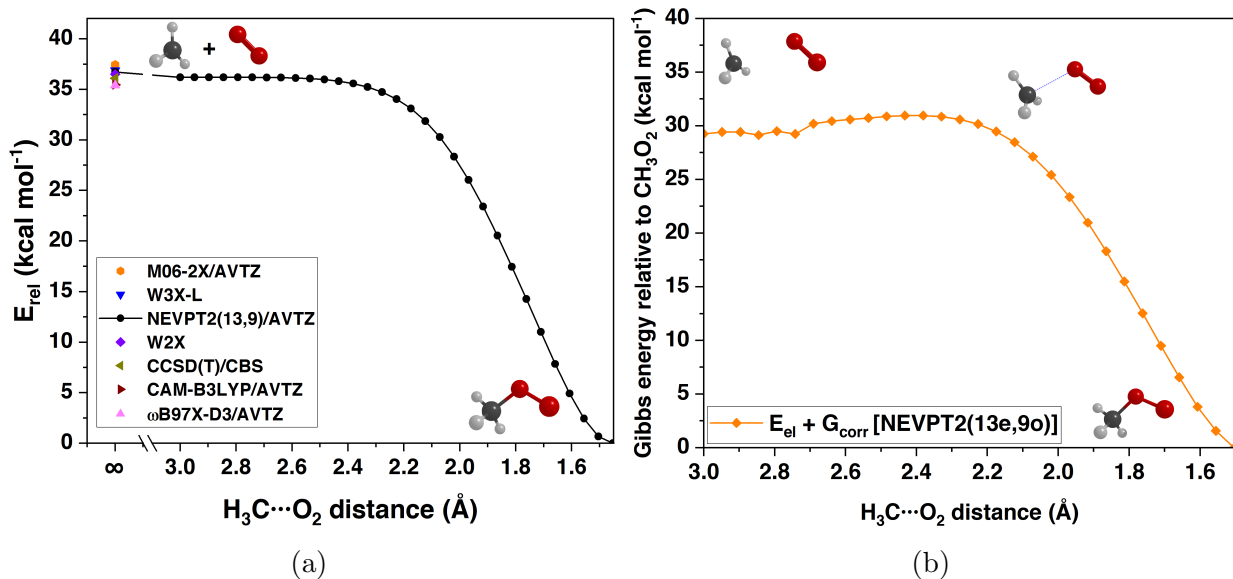


Fig. S1: a) Minimum energy path of the  $\text{CH}_3 + \text{O}_2 \rightarrow \text{CH}_3\text{O}_2$  reaction as a function of the  $\text{H}_3\text{C}\cdots\text{O}_2$  distance. b) Corresponding Gibbs energy surface, at 298K and 1 atm. Gradient of the potential projected out and the C-O torsion treated as a hindered rotation. Electronic energies and thermodynamic corrections obtained at NEVPT2(13e,9o) level.

## S2 High-pressure limit thermal rate coefficient calculations with the canonical variational theory

In canonical variational theory (CVT),<sup>1</sup> the transition state is located at the maximum of free energy along the minimum energy path of the reaction coordinate  $s$ . For reactions with an appreciable barrier in the PES( $s$ ), the maximum free energy point often coincides with the saddle point in the PES; however, for reactions with negligible or no saddle points, the location of the free energy maximum is not immediately clear.

By assigning the transition state at the maximum of the free energy, the value of the free energy of activation is simultaneously maximized, which in turn leads to the minimum value of the high-pressure limit thermal rate coefficient – the CVT rate coefficient:

$$k_{\infty}^{\text{CVT}}(T, s) = \kappa \frac{k_B T}{h} \left( \frac{p^{\ominus}}{k_B T} \right)^{1-M} \exp(-\Delta G(s)^{\ddagger, \text{CVT}} / k_B T) \quad (1)$$

$$\Delta G(s)^{\ddagger, CVT} = \max_s(G(s)_{TS}) - G(s)_{reac} \quad (2)$$

In CVT, the maximum of free energy is obtained variationally. In this work, we calculated the free energies along sampled points of the PES( $s$ ), and chose the apparent saddle point from the resulting free energy surface for the rate coefficient calculations; therefore, the free energy maximum was not obtained variationally, but the method is otherwise identical.

## S2.1 Gibbs energy surfaces of $\text{NH}_2 + \text{O}_2 \longrightarrow \text{NH}_2\text{O}_2$ and $\text{CH}_3 + \text{O}_2 \longrightarrow \text{CH}_3\text{O}_2$ reactions

The partition functions required for the Gibbs energies and the subsequent Gibbs energy surfaces of the  $\text{NH}_2 + \text{O}_2 \longrightarrow \text{NH}_2\text{O}_2$  and  $\text{CH}_3 + \text{O}_2 \longrightarrow \text{CH}_3\text{O}_2$  reactions were obtained with a rigid-rotor harmonic oscillator and hindered rotation model. In this model, other vibrations were treated as harmonic oscillators, but the torsion around the N-O and C-O bonds were estimated with a rigid one-dimensional hindered rotor model. Moreover, the hindered rotor was assumed to be uncoupled from the other vibrational modes. The vibrational entropies of low-frequency vibrations were corrected with the qRRHO model, using a  $100 \text{ cm}^{-1}$  reference value for the weighting function between the vibrational and rotational entropies.<sup>2</sup> The translational, rotational, and electronic partition functions were calculated using the standard ideal gas (trans) and rigid-rotor approximations (rot), and assuming that only the ground state contributes to the electronic partition function.

### S2.1.1 Harmonic vibrational analysis along the reaction coordinate

The harmonic vibrational analysis was carried out in all sampled points of the PES( $s$ ). The input data for the vibrational analysis are the Cartesian coordinates  $\mathbf{x}$  ( $3N \times 1$ ), Cartesian gradient  $\mathbf{g}_x$  ( $3N \times 1$ ), the Cartesian Hessian  $\mathbf{F}_x$  ( $3N \times 3N$ ), and the diagonal matrix of atomic mass triplets  $\mathbf{M}$  ( $3N \times 3N$ ). However, we carried out the vibrational analyses using internal coordinates  $\mathbf{q}$  ( $K \times 1$ ), ( $K = 3N - 6(5)$ ). The non-redundant internal coordinates

used in this work are shown in Fig. S2.

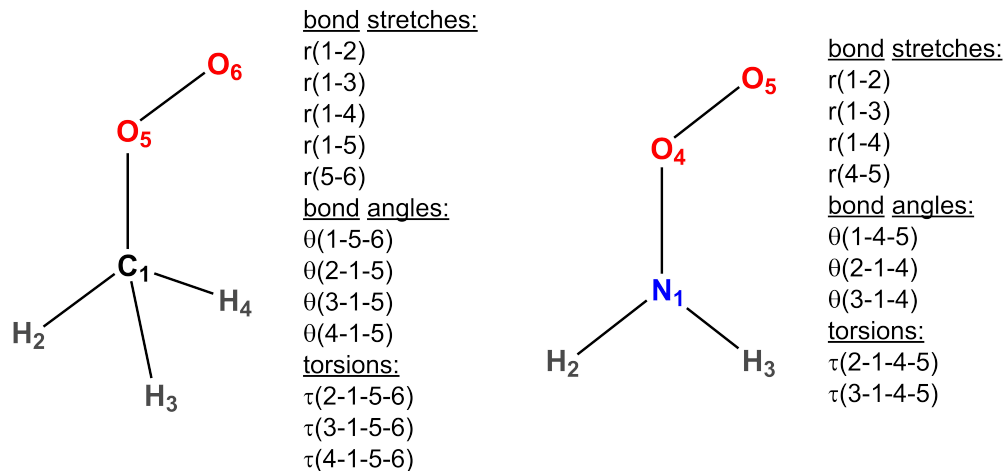


Fig. S2: Non-redundant internal coordinates used in present work.

The relationship between  $\mathbf{x}$  and internal coordinates  $\mathbf{q}$  is given by the Wilson  $\mathbf{B}$  ( $K \times 3N$ ) matrix (also the inverse Jacobian),<sup>3</sup> whose elements are defined as

$$B_{ij} = \frac{\partial q_i}{\partial x_j} \quad (3)$$

where the  $q_i$  is an internal coordinate, and  $x_j$  is a Cartesian displacement coordinate. At non-stationary points along the MEP( $s$ ), where the gradient is non-zero, to transform the Hessian to internal coordinates, the second derivatives of the internal coordinates with respect to the Cartesian displacements – the  $\mathbf{C}$  tensor ( $K \times 3N \times 3N$ ) – is also required.<sup>4,5</sup> Its elements are given by

$$C_{ijk} = \frac{\partial^2 q_i}{\partial x_j \partial x_k} \quad (4)$$

The  $\mathbf{B}$  matrices and  $\mathbf{C}$  tensors were obtained using an in-house code, in which the equations from Bakken&Helgaker (2002),<sup>5</sup> to solve the eqns. 3 and 4, are implemented. The

Cartesian Hessian is transformed to internal coordinates by

$$\mathbf{F}_{\mathbf{q}} = \mathbf{A}^T \mathbf{F}_{\mathbf{x}} \mathbf{A} - \sum_i^K \mathbf{g}_{\mathbf{q}}^{[i]} \mathbf{A}^T \mathbf{C}^{[i]} \mathbf{A} \quad (5)$$

where  $\mathbf{A}$  ( $3N \times K$ ) is the generalized inverse of the rectangular  $\mathbf{B}$  matrix,

$$\mathbf{A} = \mathbf{M}^{-1} \mathbf{B}^T (\mathbf{B} \mathbf{M}^{-1} \mathbf{B}^T)^{-1} \quad (6)$$

$\mathbf{g}_{\mathbf{q}}^{[i]}$  is the gradient with respect to the  $i^{\text{th}}$  internal coordinate, and the full gradient in internal coordinates is obtained from the Cartesian gradient via

$$\mathbf{g}_{\mathbf{q}} = \mathbf{A}^T \mathbf{g}_{\mathbf{x}} \quad (7)$$

and  $\mathbf{C}^{[i]}$  is a  $1 \times 3N \times 3N$  slice of the  $\mathbf{C}$  tensor corresponding to the  $i^{\text{th}}$  internal coordinate.

At non-stationary points on the PES, the gradient is projected out prior to diagonalization. The projector  $\mathbf{p}_{\mathbf{q}}$  is defined as:<sup>4</sup>

$$\mathbf{p}_{\mathbf{q}} = \frac{\mathbf{g}_{\mathbf{q}} \mathbf{g}_{\mathbf{q}}^T}{\mathbf{g}_{\mathbf{q}}^T (\mathbf{B} \mathbf{M}^{-1} \mathbf{B}^T) \mathbf{g}_{\mathbf{q}}}, \quad \mathbf{p}_{\mathbf{q}} = \mathbf{p}_{\mathbf{q}}^T \quad (8)$$

Then, the gradient-projected Hessian  $\mathbf{F}_{\mathbf{q}}^{\mathbf{p}}$  is obtained via

$$\mathbf{F}_{\mathbf{q}}^{\mathbf{p}} = \{\mathbf{1} - \mathbf{p}_{\mathbf{q}} \mathbf{B} \mathbf{M}^{-1} \mathbf{B}^T\} \mathbf{F}_{\mathbf{q}} \{\mathbf{1} - \mathbf{B} \mathbf{M}^{-1} \mathbf{B}^T \mathbf{p}_{\mathbf{q}}\} \quad (9)$$

The vibrational frequencies are calculated by diagonalizing the Wilson's  $\mathbf{GF}$  matrix:<sup>3,4</sup>

$$(\mathbf{GF})\mathbf{L} = \mathbf{L}\mathbf{\Lambda}, \quad \text{where } \mathbf{G} \equiv \mathbf{B} \mathbf{M}^{-1} \mathbf{B}^T, \quad \text{and } \mathbf{F} \equiv \mathbf{F}_{\mathbf{q}}^{\mathbf{p}} \quad (10)$$

where  $\mathbf{L}$  is the eigenvector matrix of normal modes, and  $\mathbf{\Lambda}$  is the diagonal eigenvalue matrix, whose elements  $\lambda_i$  (in units of  $\frac{E_h}{a_0^2 u}$ ) correspond to the  $K$  normal mode frequencies:  $\nu_i = \frac{\sqrt{\lambda_i}}{2\pi}$ .

### S2.1.2 Hindered internal rotation of the N-O and C-O bonds

The internal torsion was treated using a one-dimensional hindered rotor model by calculating the potential energy surface with respect to the torsional angle  $\theta$ ,  $V(\theta, s)$ , at each obtained value of  $s$ . The  $V(\theta, s)$  were obtained via rigid-scan, i.e. the only internal degree of freedom that was varied was the torsional angle  $\theta$ . Consequently, the torsional barriers are slightly overestimated (no relaxation), and the reduced moment of inertia ( $I_{red}$ ) remains constant during the rotation; hence, its value is independent of  $\theta$  (but not of  $s$ ), and the Hamiltonian matrix elements of the internal torsion can be obtained by integrating the hindered-rotor Hamiltonian (eqn. 12) in the basis of 1D rigid-rotor eigenfunctions. Diagonalization of the Hamiltonian yields the torsional energies, and the torsional partition function is then calculated from the sum over states and subsequently converted to internal energy and entropy.<sup>6</sup> The torsional mode was also approximated as uncoupled from the other vibrational modes.

The workflow for the treatment of the internal torsion is summarized below:

1. The studied  $\text{NH}_2\cdots\text{O}_2$  and  $\text{CH}_3\cdots\text{O}_2$  supermolecules were first symmetrized to  $C_s$ -symmetry (this ensures symmetric hindrance potential). This simplification was justified, because the converged geometries were very close to this symmetry, even though no symmetry was enforced during the geometry optimizations. The potentials  $V(\theta, s)$  were obtained with 20-point rigid scans, where the only internal coordinate that is changed is the angle  $\theta$ , which was rotated by a total of  $\pi$  radians in the 20-point scan. The full  $[0, 2\pi)$  rotation period was then obtained by mirroring the calculated  $[0, \pi]$  segment to the remaining  $(\pi, 2\pi)$  domain. The torsional potentials as a function of the N-O and C-O distances are shown in Figure S3.
2. The reduced moment of inertia,  $I_{red}(s)$  was calculated from the distances to the line defined by the N-O and C-O bonds (corresponds to  $I^{(2,1)}$  moment of inertia, using the East&Radom notation.<sup>7</sup>)

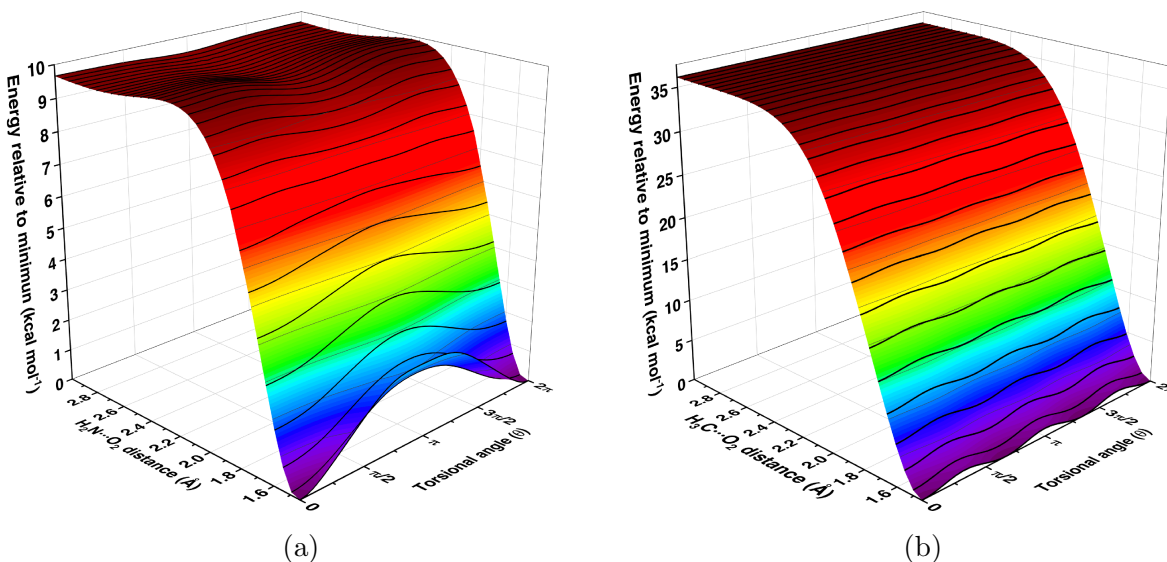
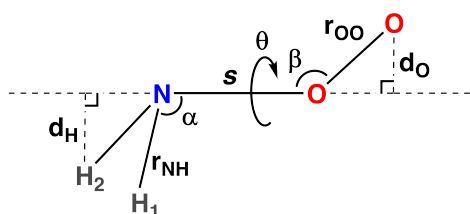


Fig. S3: Torsional potential as a function of a) N-O distance in  $\text{NH}_2\text{O}_2$ , and b) C-O distance in  $\text{CH}_3\text{O}_2$ .



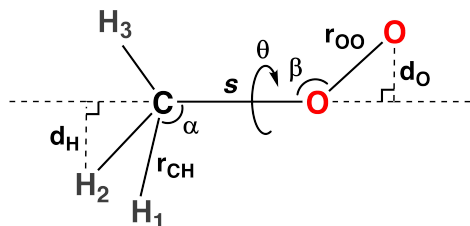
$$I_{2\text{H}} = 2m_{\text{H}}d_{\text{H}}^2 = 2m_{\text{H}}(r_{\text{NH}}\sin(\pi-\alpha))^2 \quad (\alpha > 90^\circ)$$

$$(r_{\text{NH}}\sin(\alpha))^2 \quad (\alpha < 90^\circ)$$

$$I_{\text{O}} = m_{\text{O}}d_{\text{O}}^2 = m_{\text{O}}(r_{\text{OO}}\sin(\pi-\beta))^2$$

$$I_{\text{red}} = \frac{I_{2\text{H}} \times I_{\text{O}}}{I_{2\text{H}} + I_{\text{O}}}$$

(a)



$$I_{3\text{H}} = 3m_{\text{H}}d_{\text{H}}^2 = 3m_{\text{H}}(r_{\text{NH}}\sin(\pi-\alpha))^2 \quad (\alpha > 90^\circ)$$

$$I_{\text{O}} = m_{\text{O}}d_{\text{O}}^2 = m_{\text{O}}(r_{\text{OO}}\sin(\pi-\beta))^2$$

$$I_{\text{red}} = \frac{I_{3\text{H}} \times I_{\text{O}}}{I_{3\text{H}} + I_{\text{O}}}$$

(b)

Fig. S4: Definition of the reduced moment of inertia in the a)  $\text{H}_2\text{N}-\text{O}_2$  supermolecule, and b)  $\text{H}_3\text{C}-\text{O}_2$  supermolecule.  $r_{\text{NH}_1}=r_{\text{NH}_2}$  and  $r_{\text{CH}_1}=r_{\text{CH}_2}=r_{\text{CH}_3}$  due to  $C_s$ -symmetrization.

3. The  $V(\theta, s)$  were approximated with Fourier series of 18 expansion terms (no sine terms required due to symmetry):

$$V(\theta, s) \approx F(\theta, s) = \sum_{n=0}^{18} F_n \cos(n\theta) \quad (11)$$

where the coefficients ( $F_n$ ) are obtained by projection of  $V(\theta, s)$  onto the expansion functions in the interval  $[0, 2\pi)$ . The potential could be approximated with lesser terms, but a larger number of Fourier terms ensures that the torsional partition function is converged (Table S1). The Fourier functions are plotted for selected points in Fig. S5. The hindered rotor approximation appears to be valid for other structures except for the  $\text{H}_3\text{C}-\text{O}_2$  transition state, where the internal rotation is almost barrierless ( $14 \text{ cm}^{-1}$  barrier). The black contour lines in Fig. S3b demonstrate that the methyl-torsion becomes effectively barrierless at C-O distances longer than  $2.0 \text{ \AA}$ . Therefore, we used a free rotor partition function for calculating the Gibbs energy of the internal rotation motion at the  $\text{H}_3\text{C}-\text{O}_2$  transition state.

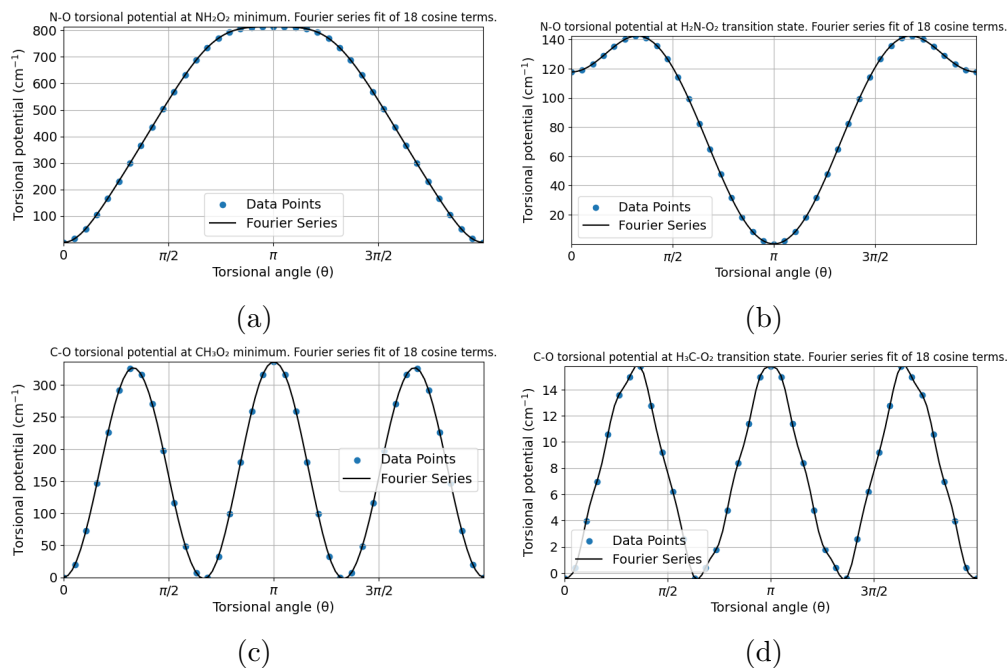


Fig. S5: Fourier fits of the torsional potentials at a)  $\text{NH}_2\text{O}_2$  minimum, b)  $\text{H}_2\text{N}-\text{O}_2$  transition state, c)  $\text{CH}_3\text{O}_2$  minimum, and d)  $\text{H}_3\text{C}-\text{O}_2$  transition state.

4. Energy states of the internal torsion are calculated by diagonalizing the matrix of the Hamiltonian operator:

$$\hat{\mathcal{H}}_{rot}(s) = -\frac{\hbar^2}{2I_{red}(s)} \frac{d^2}{d\theta^2} + F(\theta, s) \quad (12)$$

which in the 1D rigid-rotor eigenfunction basis yields following matrix elements:

$$H_{nk} = \frac{\hbar^2}{2I_{red}} k^2 + F_0 \quad \text{when } n=k \quad (13)$$

$$= \frac{F_{|n-k|}}{2} \quad \text{when } n \neq k \quad (14)$$

These elements define a 37-by-37 symmetric banded square-matrix (the bandwidth is defined by the number of Fourier series coefficients :  $2n_{max}+1$ ), whose diagonalization yields the torsional energies  $\varepsilon_j$ .

5. The torsional partition function is obtained with torsional eigenvalue summation:<sup>6</sup>

$$q_{tor} = \sum_{j=1}^{37} e^{-\frac{\varepsilon_j}{k_B T}} \quad (15)$$

6. The internal energy and entropy of the torsion were calculated with

$$U_{tor} = k_B T^2 \times \frac{d \ln q_{tor}}{dT} = \frac{\sum_{j=1}^{37} \varepsilon_j \exp(-\varepsilon_j/k_B T)}{\sum_{j=1}^{37} \exp(-\varepsilon_j/k_B T)} \quad (16)$$

$$S_{tor} = k_B \ln q_{tor} + \frac{U_{tor}}{T} \quad (17)$$

**Table S1: Convergence of the torsional partition function at 298 K as a function of number of Fourier terms used for  $V(\theta)$ .**

# Fourier terms	$q_{\text{tor}}$ of $\text{NH}_2\text{O}_2$ minimum	$q_{\text{tor}}$ of $\text{NH}_2\text{-O}_2$ TS	$q_{\text{tor}}$ of $\text{NH}_2 + \text{O}_2$ 3Å separation
1	0.270589674	1.864517783	2.362706227
2	0.736581008	2.702895476	3.376235807
3	0.941166423	3.104293035	3.852386846
4	0.996262804	3.238033874	4.013354648
5	1.01287889	3.271057921	4.052328938
6	1.015665753	3.276903605	4.059085955
7	1.01605981	3.277647295	4.059924077
8	1.01610734	3.277715247	4.059998423
9	1.016111668	3.277719707	4.060003137
10	1.016112007	3.277719918	4.060003351
11	1.016112055	3.277719925	4.060003359
12	1.016112064	3.277719925	4.060003359
13	1.016112065	3.277719925	4.060003359
⋮	⋮	⋮	⋮
20	1.016112065	3.277719925	4.060003359
⋮	⋮	⋮	⋮
28	1.016112065	3.277719925	4.060003359
29	1.016112066	3.277719925	4.060003359
30	1.016112067	3.277719925	4.060003359
31	1.016112079	3.277719925	4.060003359
32	1.016112197	3.277719925	4.060003359
33	1.016112584	3.277719937	4.060003359
34	1.016113884	3.277719942	4.060003361
35	1.016139403	3.277720168	4.060003406
36	1.016146207	3.277731983	4.060005296
37	1.016735174	3.278080581	4.060024835
38	1.04058264	3.279698654	4.060414716
39	1.084840526	3.289638486	4.06270343

## S3 Details of the Master Equation simulations with MESMER

The Master Equation (ME) simulations were done using the RRKM and ILT methods for obtaining the microcanonical rate coefficients. These methodologies are briefly discussed below, before going into the details of the ME simulation results. The ME simulations were done using pseudo-first order conditions, where  $\text{O}_2$  was the excess reactant,  $\text{CH}_3$  and  $\text{NH}_2$  the deficient reactant, and  $\text{CH}_3\text{O}_2$  and  $\text{NH}_2\text{O}_2$  were modelled. We used the default Lennard-Jones parameters ( $\varepsilon/k = 50$  K,  $\sigma = 5$  Å) for the modelled compounds in the ME simulations. We ran a sensitivity test with LJ-parameters calculated with the Joback method,<sup>8,9</sup> with which we obtained  $\varepsilon/k = 517$  K,  $\sigma = 3.67$  Å for  $\text{NH}_2\text{O}_2$ , but an ILT/ME with these values makes negligible difference to  $k_f$  wrt. default settings. For the  $\text{N}_2$  bath gas, we used  $\varepsilon/k = 91.9$  K,  $\sigma = 3.92$  Å. A  $50 \text{ cm}^{-1}$  grain size and  $20 kT$  energy above the highest stationary point was used in all ME simulations. We used  $\text{O}_2$  concentration equal to 21% of the total pressure to mimic atmospheric oxygen levels. The Bartis-Widom phenomenological rate coefficients corresponding to pseudo-first order  $\text{NH}_2$  and  $\text{CH}_3$  losses were converted to bimolecular rate coefficients by dividing the pseudo-first order coefficients with the oxygen concentration.

### S3.1 RRKM simulations

The RRKM theory is strictly defined only for unimolecular processes; therefore, to model a bimolecular reaction with RRKM method requires a two-step procedure: an association step to form a pre-reactive complex (PRC) from the reactants,  $\text{R} + \text{O}_2 \longrightarrow \text{R}\dots\text{O}_2$ , whose unimolecular isomerization to  $\text{RO}_2$  through a transition state may then be modelled with RRKM. The PRC formation was modelled with ILT, using a pre-exponential factor of  $A = 10^{-10} \text{ cm}^3 \text{ molecule}^{-1} \text{ s}^{-1}$  and zero activation energy. The transition state structures were obtained with the CVT method.

The reaction potential for the  $\text{NH}_2 + \text{O}_2 \longrightarrow \text{NH}_2\text{O}_2$  obtained at the NEVPT2(13e,11o) level showed a shallow a PRC, which enabled the use of RRKM. However, after the electronic energies were corrected at the NEVPT2(19e,14o) level, the PRC was no longer a minimum on the PES. We also used the W3X-L method for calculating the energy of the PRC, at the NEVPT2(13e,11o) geometry. However, we were not able to obtain correct doublet reference state for the calculations, so the calculations were done using quartet multiplicity instead. The energy difference between the true doublet state and the quartet state should be rather small. The energy difference between the lowest doublet and quartet states ( $\Delta E_{Q_0 \leftarrow D_0}$ ) at NEVPT2(19e,14o)//NEVPT2(13e,11o) is about 1.8 kcal mol<sup>-1</sup>, so the W3X-L energy of the quartet pre-reactive complex is likely higher than the doublet state by comparable amount. For comparison, at the transition state, the  $\Delta E_{Q_0 \leftarrow D_0}$  at NEVPT2(19e,14o) is already 9.0 kcal mol<sup>-1</sup>, hence the transition state could not be approximated with a quartet state.

We ran into issues, when we calculated the relative E+ZPEs of the stationary points for the MESMER calculations: the PRC was slightly above the reactants in E+ZPE (but below the transition state). We set E+ZPE of the PRC to be equal to that of the reactants and ran the simulation. Then, we ran a sensitivity test by lowering the E+ZPE of the PRC with 1.0 kcal mol<sup>-1</sup> below the reactants and found no effect on the association reaction rate coefficient. Furthermore, we ran another simulation, where the PRC formation step was removed completely, and the RRKM was run directly from the reactants, through the TS, to the peroxy radical product. Interestingly, this approach yielded almost identical results to the above methods. For the  $\text{CH}_3 + \text{O}_2 \longrightarrow \text{CH}_3\text{O}_2$  system, no pre-reactive complex was found, so we only used the direct bimolecular RRKM described above. We do recognize that the validity of these bimolecular RRKM simulations are not well rooted in theory, which is why we mostly concentrate on our ILT results.

### S3.2 ILT simulations

The ILT simulations only require prior knowledge of the high-pressure limit Arrhenius parameters, and do not necessarily require any information of the transition states. However, in our approach, the Arrhenius parameters (Fig. S6) are derived from the calculated  $k_{\infty}^{CVT}$  values, which explicitly depend on the definition of the transition state.

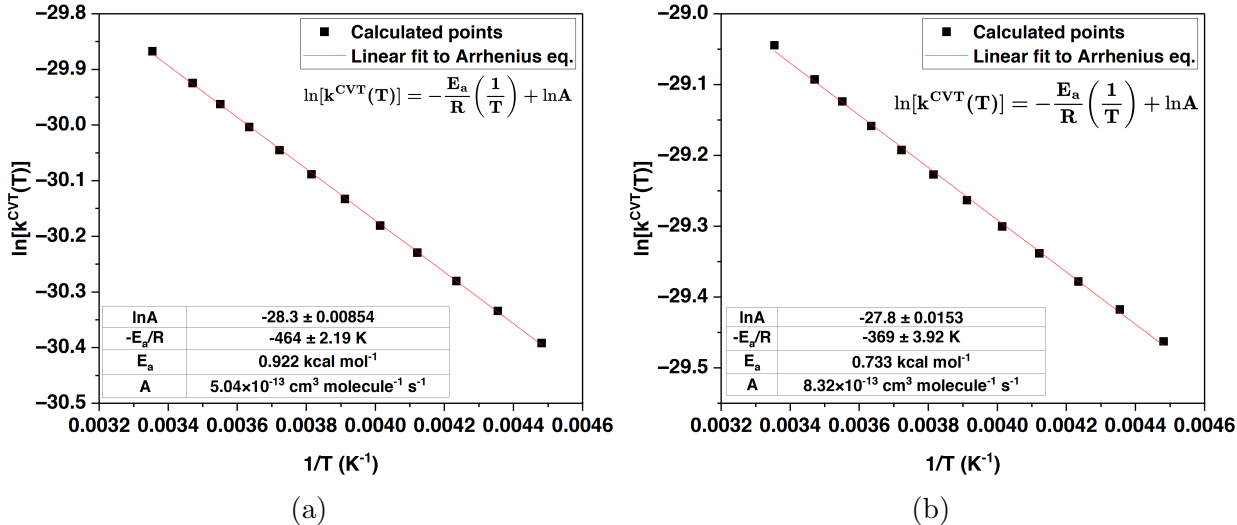


Fig. S6: Arrhenius fits of the  $k_{\infty}^{CVT}$  rate coefficients for a)  $\text{NH}_2 + \text{O}_2 \longrightarrow \text{NH}_2\text{O}_2$ , and b)  $\text{CH}_3 + \text{O}_2 \longrightarrow \text{CH}_3\text{O}_2$ .

### S3.3 ME results

The ME simulations were done using various temperatures and pressures to investigate the p,T dependence of the  $\text{NH}_2 + \text{O}_2 \xrightleftharpoons[k_r]{k_f} \text{NH}_2\text{O}_2$  equilibrium (and  $\text{CH}_3 + \text{O}_2 \xrightleftharpoons[k_r]{k_f} \text{CH}_3\text{O}_2$  for comparison and method validation purposes). The equilibrium between the reactants and the products were reached within the timescale of the simulation, and the rate coefficients of the reverse dissociation reactions ( $k_r$ ) were obtained from the pseudo-first order rate coefficients of the forward reaction ( $k'_f = k_f[\text{O}_2]$ ) with the detailed balance:

$$K_{eq} = \frac{k'_f}{k_r} \implies k_r = \frac{k'_f}{K_{eq}} \quad (18)$$

Fig. S7 shows the pressure dependencies of the forward and reverse reaction rate coefficients in different temperatures. At 1 bar pressure, the  $\text{NH}_2 + \text{O}_2 \longrightarrow \text{NH}_2\text{O}_2$  reaction rate coefficient is about two orders of magnitude smaller than at the high-pressure limit (HPL), while the  $\text{CH}_3 + \text{O}_2 \longrightarrow \text{CH}_3\text{O}_2$  is very close to HPL already at 1 bar pressure. At their respective HPL, the rate coefficients of the  $\text{NH}_2 + \text{O}_2 \longrightarrow \text{NH}_2\text{O}_2$  and  $\text{CH}_3 + \text{O}_2 \longrightarrow \text{CH}_3\text{O}_2$  are quite similar, which is not that surprising, given that these reactions are highly analogous.

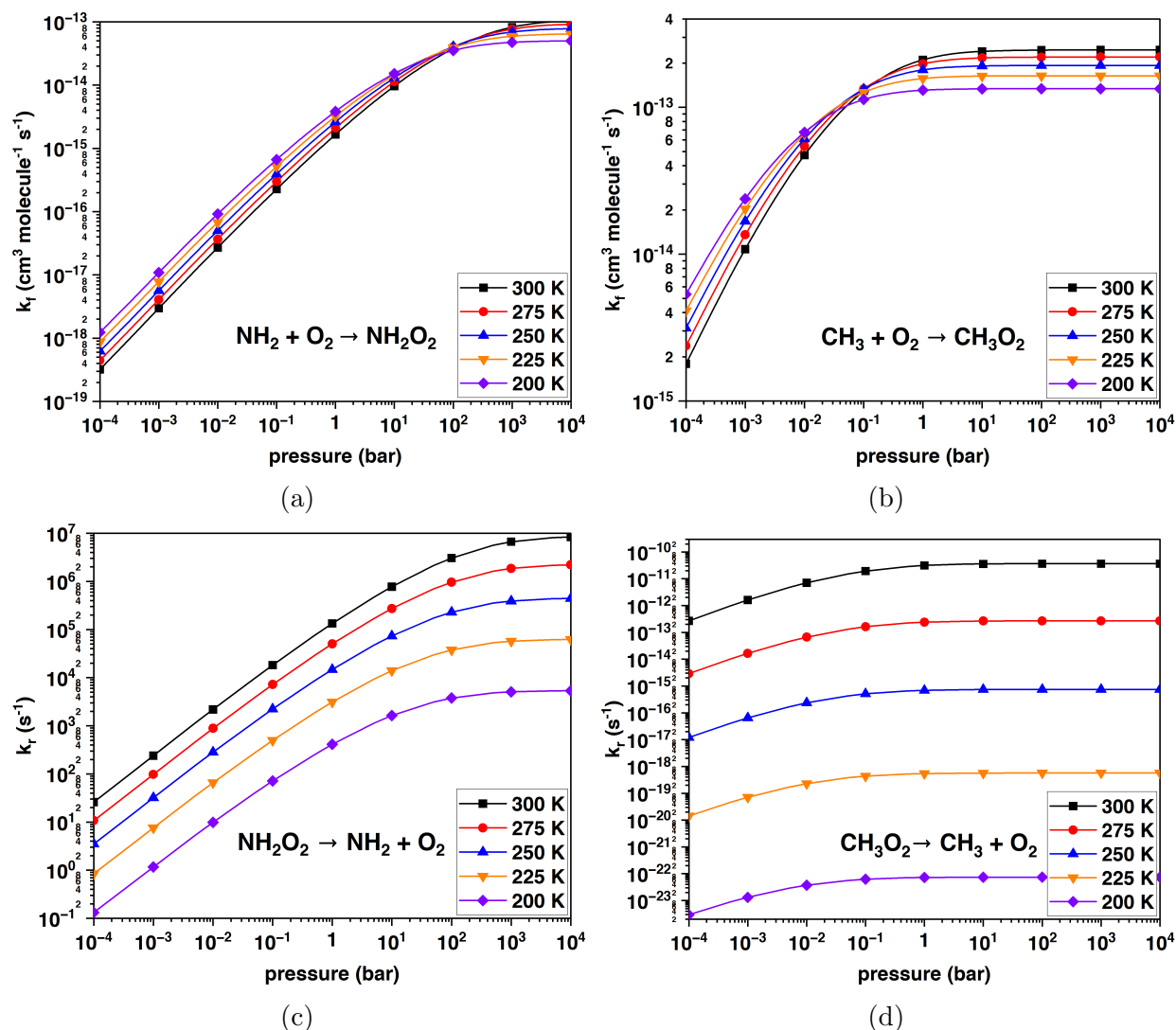


Fig. S7: Pressure dependence of the reaction rate coefficients, in the pressure range of  $10^{-4}$ – $10^4$  bar, at temperatures of 300 K (black), 275 K (red), 250 K (blue), 225 K (orange), and 200 K (violet). a)  $\text{NH}_2 + \text{O}_2 \longrightarrow \text{NH}_2\text{O}_2$ , b)  $\text{CH}_3 + \text{O}_2 \longrightarrow \text{CH}_3\text{O}_2$ , c)  $\text{NH}_2\text{O}_2 \longrightarrow \text{NH}_2 + \text{O}_2$ , d)  $\text{CH}_3\text{O}_2 \longrightarrow \text{CH}_3 + \text{O}_2$ . Obtained with ILT/ME.

While there are obviously uncertainties in the obtained rate coefficient values, we do not expect the uncertainty to be more than 1–2 orders of magnitude at the largest. This assessment is further supported by the obtained rate coefficients for the  $\text{CH}_3 + \text{O}_2 \longrightarrow \text{CH}_3\text{O}_2$  reaction, which are within an order of magnitude of the IUPAC estimates.<sup>10</sup> Summary of rate coefficients obtained at various methods at 298 K and 1 atm is shown in Table S2, and the equilibrium fraction of  $\text{NH}_2\text{O}_2$  at various temperatures and pressures is shown in Fig. S8.

**Table S2: MESMER results of  $\text{NH}_2 + \text{O}_2 \xrightleftharpoons[k_r]{k_f} \text{NH}_2\text{O}_2$  and  $\text{CH}_3 + \text{O}_2 \xrightleftharpoons[k_r]{k_f} \text{CH}_3\text{O}_2$  reactions, at 298 K and 1 atm.**

	ILT/ME	RRKM/ME with PRC	Bimolecular RRKM/ME
$\text{NH}_2 + \text{O}_2 \longrightarrow \text{NH}_2\text{O}_2$			
$k_f$ ( $\text{cm}^3 \text{ molecule}^{-1} \text{ s}^{-1}$ )	$1.7 \times 10^{-15}$	$2.5 \times 10^{-15}$	$2.5 \times 10^{-15}$
$k_r$ ( $\text{s}^{-1}$ )	$1.3 \times 10^5$	$1.8 \times 10^5$	$1.8 \times 10^5$
$\text{CH}_3 + \text{O}_2 \longrightarrow \text{CH}_3\text{O}_2$			
$k_f$ ( $\text{cm}^3 \text{ molecule}^{-1} \text{ s}^{-1}$ )	$2.1 \times 10^{-13}$	-	$1.1 \times 10^{-12}$
$k_r$ ( $\text{s}^{-1}$ )	$2.3 \times 10^{-11}$	-	$1.2 \times 10^{-10}$

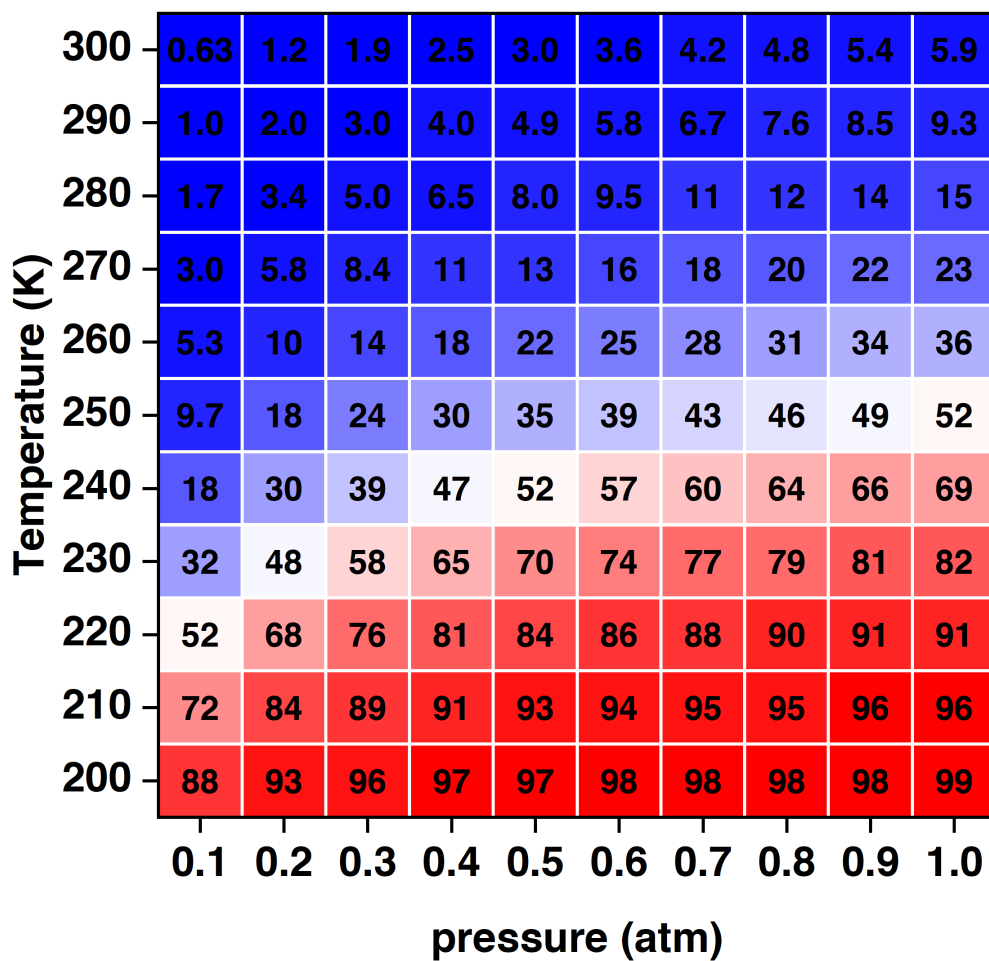


Fig. S8: Heat map of the  $\text{NH}_2\text{O}_2$  equilibrium fractions (%) as a function of the reaction conditions. Note that the partial pressure of  $\text{O}_2$  is held at constant 21% of the total pressure across all pressures, to be consistent with atmospheric conditions. Values obtained with the ILT/ME method.

### S3.4 Sensitivity tests

We carried out various sensitivity tests for the forward reaction rate coefficients,  $k_f$ . For example, we used different collisional energy transfer values (Fig. S9). Our default setting in the simulations was  $\langle \Delta E \rangle_d = 100 \text{ cm}^{-1}$ , and increasing this value only makes the association reaction faster. According to the MESMER manual,  $\text{N}_2$  and  $\text{O}_2$  tend to have  $\langle \Delta E \rangle_d$  values of 175–275  $\text{cm}^{-1}$ , so the rate coefficients in Table S2 might be slightly underestimated. We only used temperature independent model for the  $\langle \Delta E \rangle_d$ .

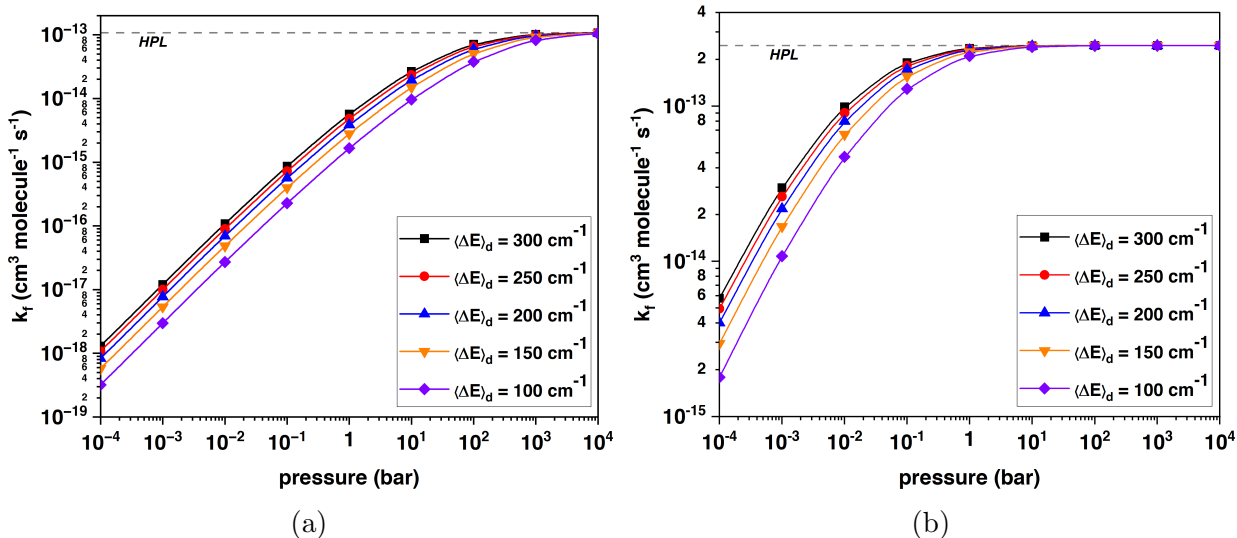


Fig. S9: Dependence of the bimolecular association reaction rate coefficient (at 300 K) on the average energy lost  $\langle \Delta E \rangle_d$  in collisions with the  $\text{N}_2$  bath: 300 (**black**), 250 (**red**), 200 (**blue**), 150 (**orange**), and 100 (**violet**), in units of  $\text{cm}^{-1}$ . a)  $\text{NH}_2 + \text{O}_2 \longrightarrow \text{NH}_2\text{O}_2$ , b)  $\text{CH}_3 + \text{O}_2 \longrightarrow \text{CH}_3\text{O}_2$ . HPL = high-pressure limit. Obtained with the ILT/ME method.

One source of uncertainty in the qualitative conclusion, whether the  $\text{NH}_2\text{O}_2$  is present in atmospheric conditions or not is the relative energy difference between the  $\text{NH}_2 + \text{O}_2$  and  $\text{NH}_2\text{O}_2$ , which is the largest deciding factor on the equilibrium fractions of  $\text{NH}_2$  vs.  $\text{NH}_2\text{O}_2$ . The  $\text{CH}_3 + \text{O}_2 \rightleftharpoons \text{CH}_3\text{O}_2$  is not as sensitive to this energy difference, as the equilibrium fraction of  $\text{CH}_3\text{O}_2$  is 100% in ambient conditions; however, the forward reaction rate coefficient is sensitive to this energy difference. The main results are obtained with the relative energy differences calculated at the W3X-L level. We shifted this relative energy difference by  $\pm 0.5 \text{ kcal mol}^{-1}$  to test how the rate coefficients vary for both  $\text{NH}_2 + \text{O}_2 \longrightarrow$

$\text{NH}_2\text{O}_2$  and  $\text{CH}_3 + \text{O}_2 \longrightarrow \text{CH}_3\text{O}_2$  (Fig. S10), and how it affects the equilibrium fractions of  $\text{NH}_2\text{O}_2$ , using the ILT/ME method (Fig. S11). Increasing the relative energy of reactants to products, while holding the energy of transition state constant, lowers the Arrhenius activation energy by the same amount, and *vice versa*.

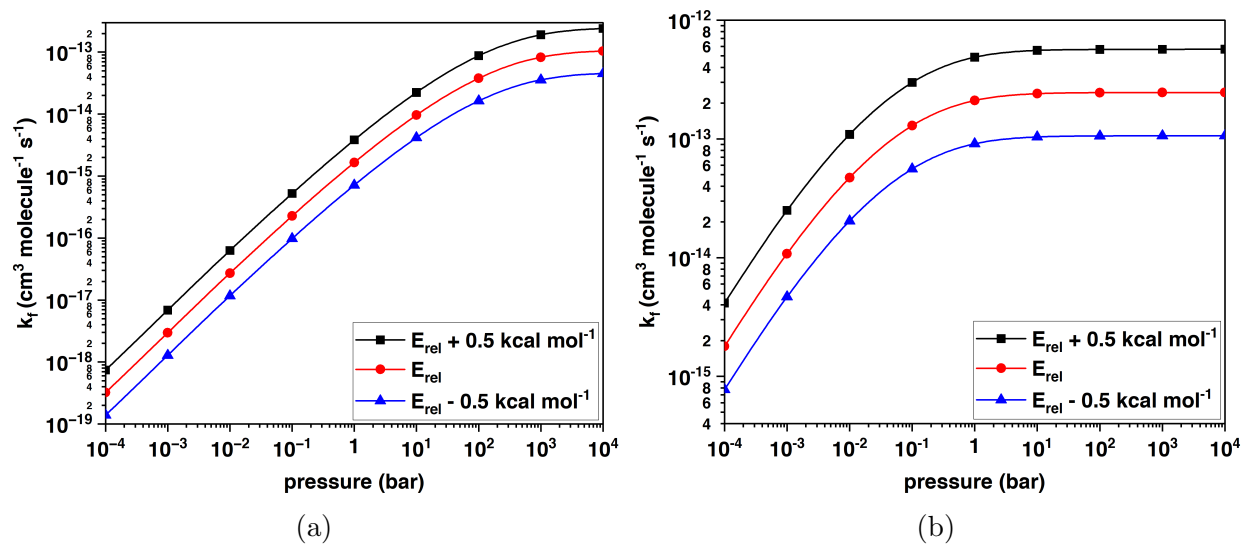


Fig. S10: Dependence of the bimolecular association reaction rate coefficient (at 300 K) on the value of the relative energy difference ( $E_{\text{rel}}$ ) between reactants and products. Original value (**red**),  $E_{\text{rel}}$  increased by  $0.5 \text{ kcal mol}^{-1}$  (**black**),  $E_{\text{rel}}$  lowered by  $0.5 \text{ kcal mol}^{-1}$  (**blue**). a)  $\text{NH}_2 + \text{O}_2 \longrightarrow \text{NH}_2\text{O}_2$ , b)  $\text{CH}_3 + \text{O}_2 \longrightarrow \text{CH}_3\text{O}_2$ . Obtained with the ILT/ME method.

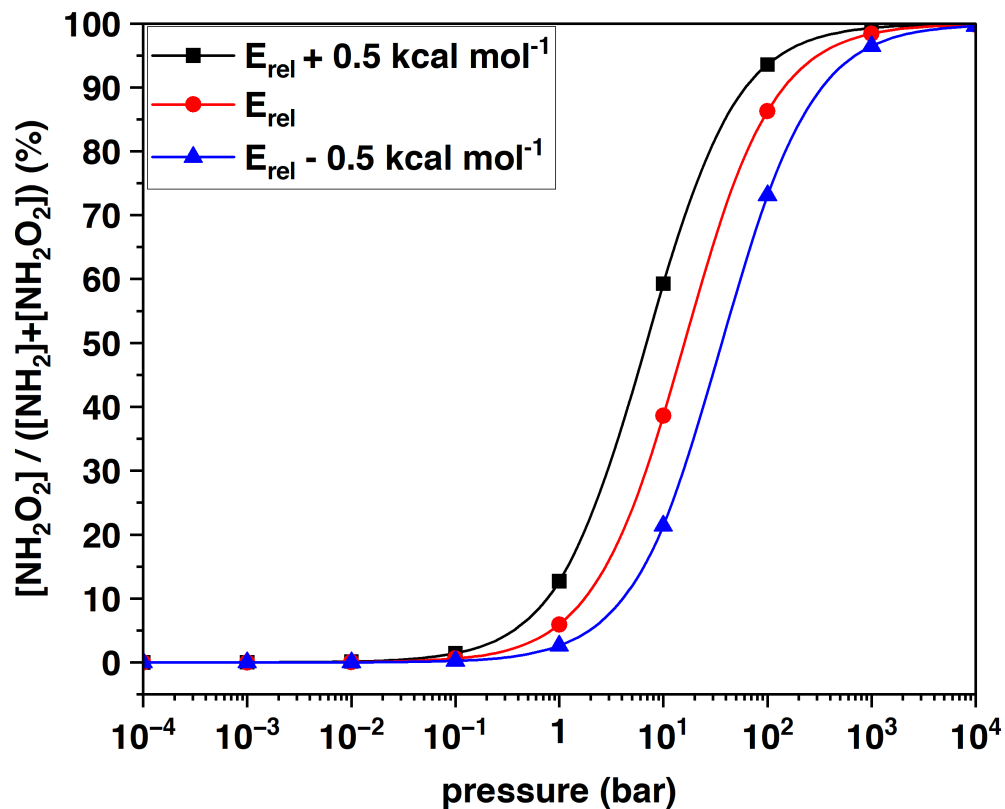


Fig. S11: Equilibrium fraction of  $\text{NH}_2\text{O}_2$  as a function of pressure and relative energy difference ( $E_{\text{rel}}$ ) between  $\text{NH}_2 + \text{O}_2$  and  $\text{O}_2$ , at 300 K. Original value (red),  $E_{\text{rel}}$  increased by  $0.5 \text{ kcal mol}^{-1}$  (black),  $E_{\text{rel}}$  lowered by  $0.5 \text{ kcal mol}^{-1}$  (blue). a)  $\text{NH}_2 + \text{O}_2 \longrightarrow \text{NH}_2\text{O}_2$ , b)  $\text{CH}_3 + \text{O}_2 \longrightarrow \text{CH}_3\text{O}_2$ . Obtained with the ILT/ME method.

Another parameter that affects the rate coefficients (but not the equilibrium fractions), is the Gibbs energy barrier height (PES is barrierless). Like discussed, this barrier height is obtained at the NEVPT2 level for the reverse reaction and the forward reaction barrier is then calculated from the W3X-L reaction Gibbs energy and the reverse reaction barrier. Figure 2a in the main article shows that the  $\Delta E$  of the  $\text{NH}_2 + \text{O}_2 \longrightarrow \text{NH}_2\text{O}_2$  reaction at NEVPT2(19e,14o) level is about  $0.8 \text{ kcal mol}^{-1}$  higher than with the W3X-L. If we assume that this difference between W3X-L and NEVPT2 is constant, the Gibbs energy barrier height can also be thought to be  $0.8 \text{ kcal mol}^{-1}$  too high. Therefore, we carried out an ILT/ME simulation with  $0.8 \text{ kcal mol}^{-1}$  lowered barrier to assess this. Without lowering the barrier height, the forward rate coefficient is  $1.7 \times 10^{-15} \text{ cm}^3 \text{ molecule}^{-1} \text{ s}^{-1}$ , while with the lowered barrier, it is  $4.6 \times 10^{-15} \text{ cm}^3 \text{ molecule}^{-1} \text{ s}^{-1}$ .

## S4 Calculated fraction of $\text{NH}_2\text{O}_2$ as a function of altitude

The temperatures and pressures at varying altitudes (Table S3) were calculated using the barometric formula:<sup>11</sup>

$$p(h) = p_0 \times \left( 1 - \frac{\alpha}{T_{surf}} h \right)^{\frac{Mg}{\alpha R}}$$

where  $p_0$  is the pressure at surface level,  $T_{surf}$  the surface temperature,  $\alpha$  the temperature lapse rate,  $h$  the altitude from surface,  $g$  the Earth's standard gravity (9.80665 m s<sup>-2</sup>),  $M$  the molar mass of air (0.0289644 kg mol<sup>-1</sup>), and  $R$  the molar gas constant. We used two surface temperature scenarios: 288 K, which corresponds to the global average surface temperature, and 263 K to represent the surface temperature of polar regions. International standard tropospheric temperature lapse rate  $\alpha=0.0065$  K m<sup>-1</sup> was used in both scenarios.<sup>12</sup>

**Table S3: Pressures and temperatures at various altitudes, calculated with the barometric formula, using two surface temperature scenarios.**

$h$ (km)	Global average $T_{surf} = 288$ K		Polar $T_{surf} = 263$ K	
	$p$ (Torr)	$T$ (K)	$p$ (Torr)	$T$ (K)
0	760	288	760	263
1	674	281.5	666	256.5
2	596	275	582	250
3	526	268.5	507	243.5
4	462	262	440	237
5	405	255.5	380	230.5
6	354	249	327	224
7	308	242.5	280	217.5
8	267	236	239	211
9	230	229.5	203	204.5
10	198	223	171	198

## S5 Calculated fraction of $\text{NH}_2\text{O}_2$ under different experimental conditions

Table S4: Calculated equilibrium fraction of  $\text{NH}_2\text{O}_2$  under different experimental reaction conditions.<sup>[a]</sup>

T (K)	$p_{\text{total}}$ (Torr)	$\text{O}_2$ %	% of $\text{NH}_2\text{O}_2$
272	240	6	2.4
348	240	6	0.08
298	100	100	2
298	570	0.18	0.04
298	570	18	4.2
298	570	100	20
350	705	42	1.5

<sup>[a]</sup> See the main article for the discussion related to these values.

## S6 $\text{NH}_2 + \text{O}_2 \rightarrow \text{NH}_2\text{O}_2$ , calculated using CASPT2 and CASPT2-IPEA

In addition to the NEVPT2 calculations, we investigated the  $\text{NH}_2 + \text{O}_2 \rightarrow \text{NH}_2\text{O}_2$  reaction also with complete active space second-order perturbation theory (CASPT2),<sup>13</sup> and its IPEA-shifted variant, CASPT2-IPEA.<sup>14</sup> The CASPT2 and CASPT2-IPEA methods are based on the generalized Fock operator, while the NEVPT2 uses a partially bielectronic Dyall’s Hamiltonian.<sup>15</sup> In CASPT2-IPEA, the denominators in the second-order perturbational energy corrections involving CAS orbital energies are substituted with an empirical parameter, IPEA-shift.<sup>14,16</sup> The CASPT2-IPEA has been shown to yield more accurate reaction energies for systems where the number of paired electrons changes during the reaction.<sup>14,17,18</sup>

The potential energy curves of the  $\text{NH}_2 + \text{O}_2 \rightarrow \text{NH}_2\text{O}_2$  reaction, obtained with the CASPT2 and CASPT2-IPEA methods, are shown in the Figure S12. The geometries are optimized at CASPT2(13e,11o)/aug-cc-pVTZ level of theory, using the same active space as in the NEVPT2 geometry optimizations discussed in the main article. The CASPT2(13e,11o)/aug-cc-pVTZ potential energy curve was obtained using relaxed scan of the  $\text{H}_2\text{N}-\text{O}_2$  bond (black trace in Figure S12). The various CASPT2-IPEA curves are obtained from single-point correction calculations on the CASPT2 optimized geometries, using different values for the IPEA-shifts (other traces in Figure S12). The obtained curves highlight the inaccuracy of canonical CASPT2 in calculating reaction energy for system where the number of unpaired electrons change ( $\star$  symbol in Figure S12 which corresponds to CCSD(T)/CBS relative energy). Furthermore, the reaction energies appear to be very sensitive to the used IPEA shift parameter, which was used in range of 0.15 to 0.50 a.u. The hollow points in Figure S12 correspond to the highest energy point located around the assumed saddle point. It is evident that increasing the IPEA-shift also shifts the saddle point to longer  $\text{H}_2\text{N}-\text{O}_2$  distance, which implies that CASPT2 optimized geometries may not be ac-

curate for reaction energy estimations, even when using the CASPT2-IPEA corrections. Due to the high sensitivity to the IPEA-shift value and large mismatch between the saddle-point location suggested by CASPT2 vs. CASPT2-IPEA, we decided to use NEVPT2 for obtaining the reaction potentials in this work. The merit of NEVPT2 in comparison to CASPT2 and CASPT2-IPEA is that it is both size-consistent and does not rely on empirical parameters (IPEA shift), which made obtaining comparable sets of energies and thermochemical parameters across multiple studied reaction pathways easier much easier with NEVPT2.

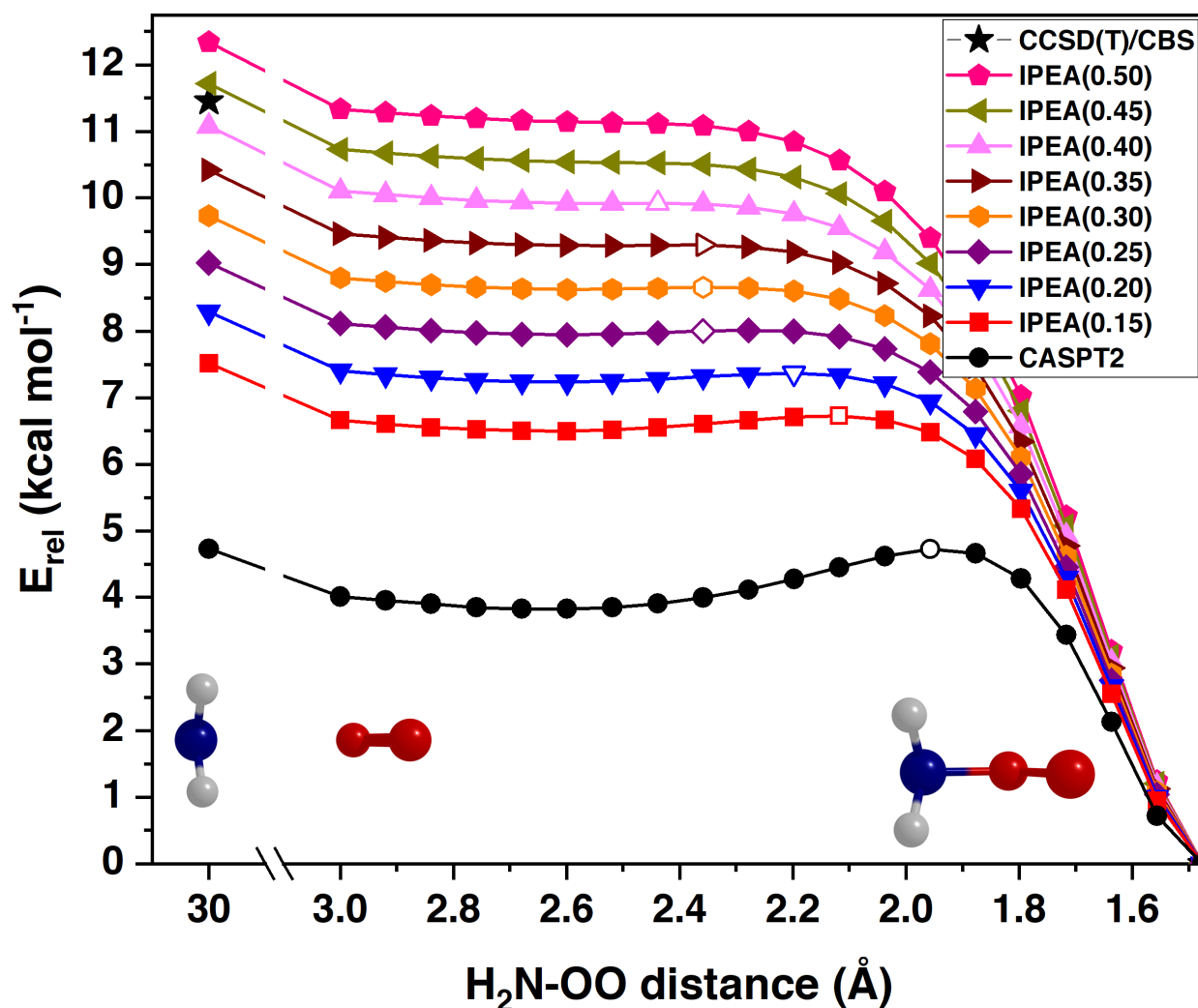


Fig. S12: Association reaction curve of  $\text{NH}_2 + \text{O}_2 \longrightarrow \text{NH}_2\text{O}_2$ , obtained using CASPT2(13e,11o)/aug-cc-pVTZ and CASPT2-IPEA//CASPT2 methods, using a range of IPEA-shift values. The CCSD(T)/CBS// $\omega$ B97X-D3/aug-cc-pVTZ relative energy is shown for comparison ( $\star$ ). The hollow points correspond to the highest energy point located around the assumed saddle point.

## S7 Comparison of ATcT database reaction enthalpies and calculated reaction enthalpies

To validate the accuracy of the theoretical methods used in the present study, we compared calculated reaction enthalpies to those available in the Active Thermochemical Tables (ATcT) database (Table S5).<sup>19,20</sup> Note that the  $\text{NH}_2\text{O}_2$  radical is not in the database; therefore, benchmark values for the reaction enthalpy of  $\text{NH}_2 + \text{O}_2 \longrightarrow \text{NH}_2\text{O}_2$  are not available. Some idea of the accuracy of the methods used in the present work can be obtained by comparing the calculated reaction enthalpies of other reactions, for which the ATcT values are available. The values obtained in this work agree well with ATcT values and there does not appear to be systematic over- or underestimations in the values compared to ATcT. In the main article, the relative electronic energy difference between  $\text{NH}_2 + \text{O}_2$  and  $\text{NH}_2\text{O}_2$  has been further corrected with the W3X-L method, which ought to be the most accurate electronic structure method used; therefore, the energetics of the  $\text{NH}_2 + \text{O}_2 \rightleftharpoons \text{NH}_2\text{O}_2$  should be even more accurate than those calculated with only at NEVPT2 and shown in the Table S5.

**Table S5: Comparison of ATcT database reaction enthalpies and calculated reaction enthalpies (at NEVPT2), in units of kcal mol<sup>-1</sup>.**

Reaction	ATcT $\Delta H_{\text{reac}}, 0 \text{ K}$	ATcT $\Delta H_{\text{reac}}, 298 \text{ K}$	NEVPT2 $\Delta H_{\text{reac}}, 0 \text{ K}$	NEVPT2 $\Delta H_{\text{reac}}, 298 \text{ K}$
$\text{NH}_2 + \text{O}_2 \longrightarrow \text{HNO} + \text{OH}$	-9.97	-9.93	-11.04	-11.04
$\text{NH}_2 + \text{O}_2 \longrightarrow \text{NO} + \text{H}_2\text{O}$	-80.59	-80.48	-79.47	-79.47
$\text{NH}_2 + \text{O}_2 \longrightarrow \text{H}_2\text{NO} + \text{O}$	30.73	30.41	30.96	30.72
$\text{CH}_3 + \text{O}_2 \longrightarrow \text{CH}_3\text{O}_2$	-30.43	-31.88	-30.22	-31.80

S8 NEVPT2 calculations: structural parameters, CAS orbitals, vibrational frequencies, and rotational constants

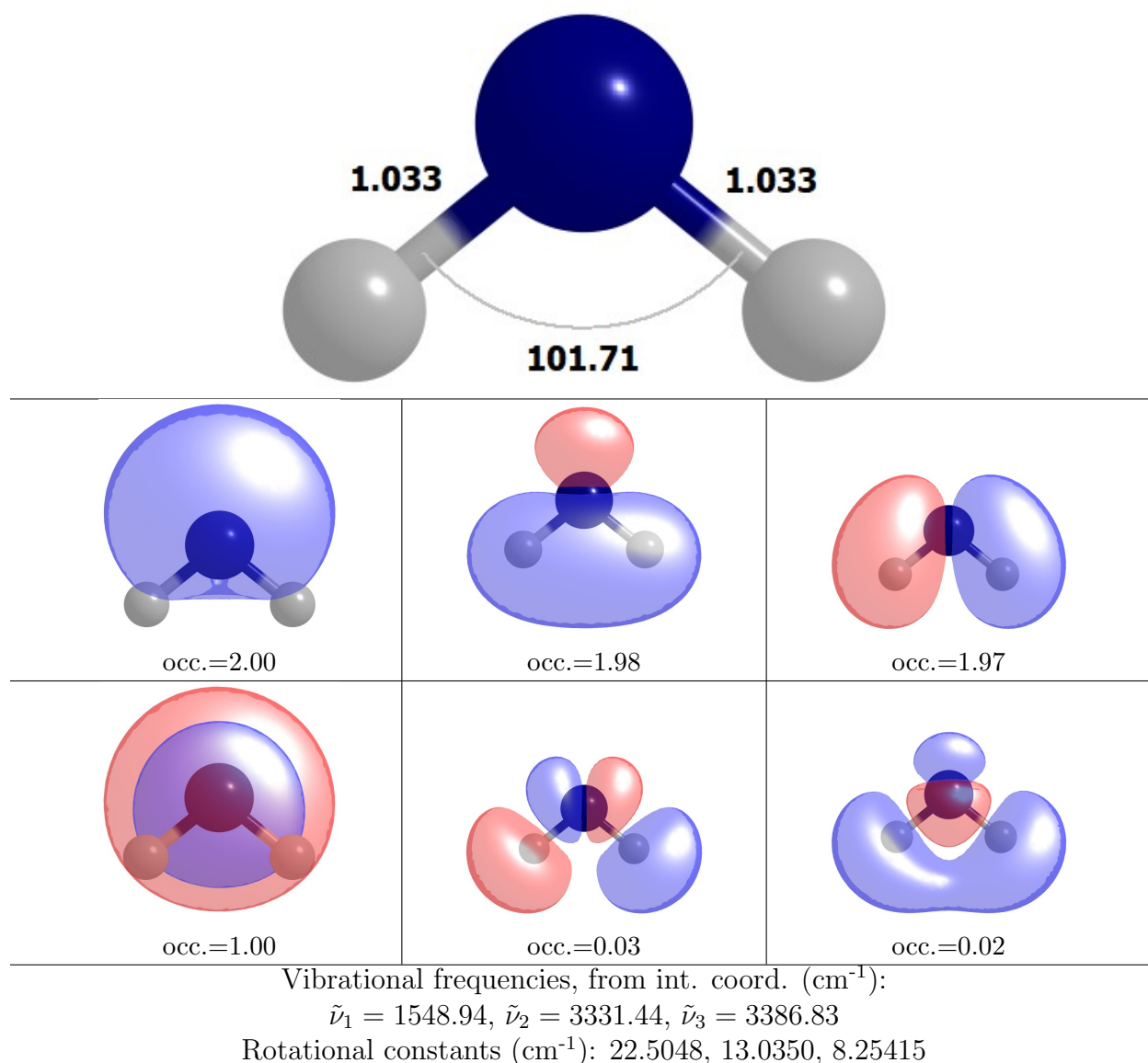
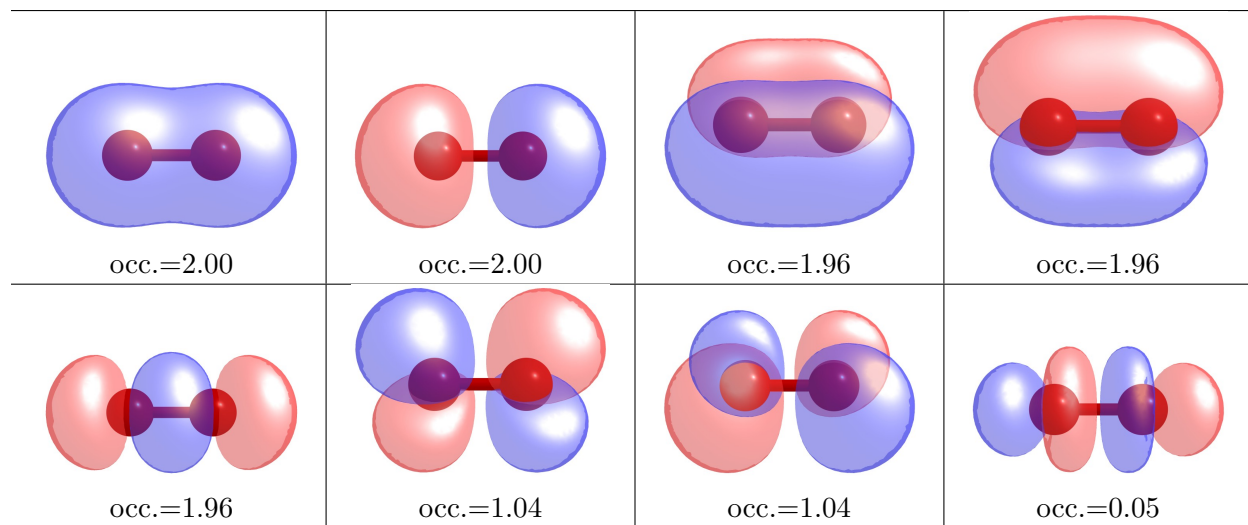
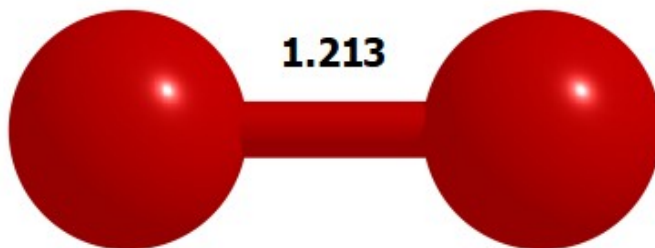


Fig. S13:  $\text{NH}_2$  ( $C_{2v}$ ), NEVPT2(7e,6o)/aug-cc-pVTZ, bond lengths in the units of Ångström.



Vibrational frequency ( $\text{cm}^{-1}$ ):

$$\tilde{\nu}_1 = 1573.70$$

Rotational constants ( $\text{cm}^{-1}$ ): 0.00000, 1.43257, 1.43257

Fig. S14:  $\text{O}_2$  ( $D_{\infty h}$ )  ${}^3\Sigma_g^-$ , NEVPT2(12e,80)/aug-cc-pVTZ, bond lengths in the units of Ångström.

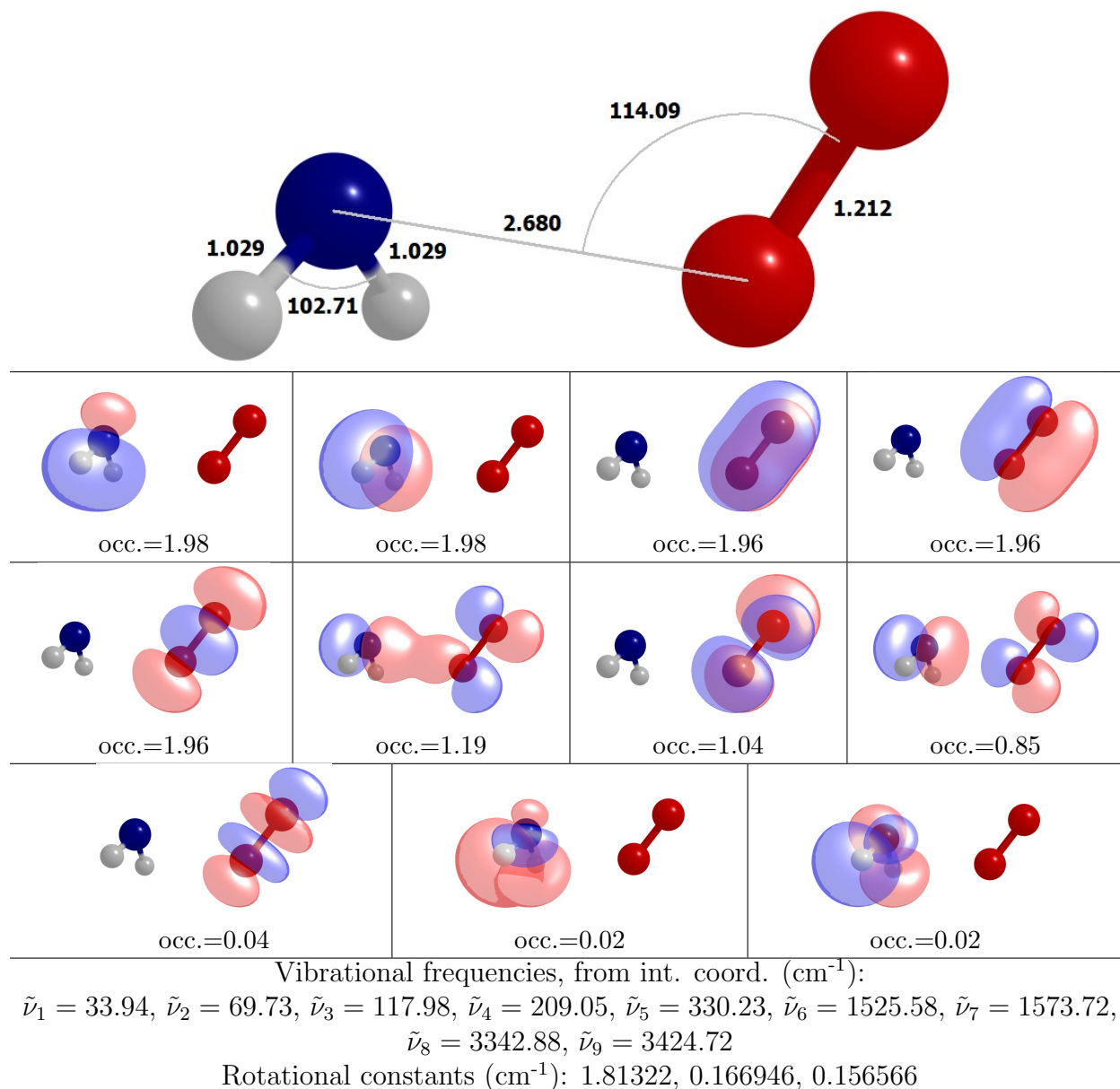
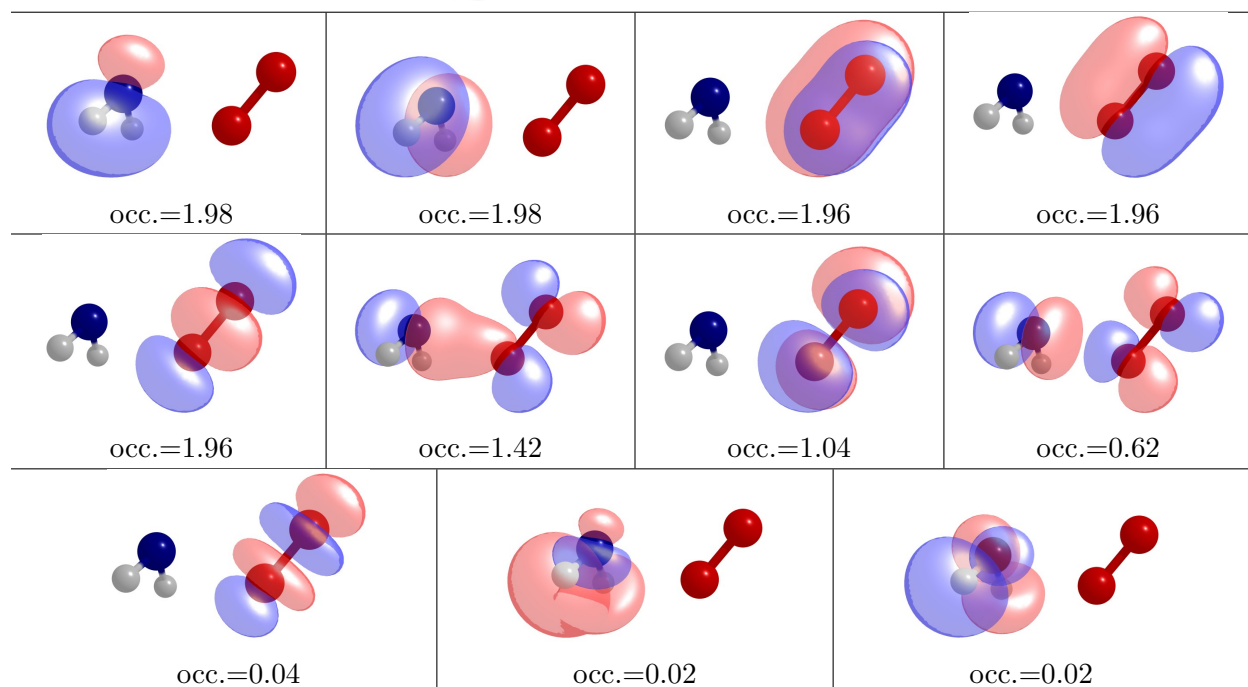
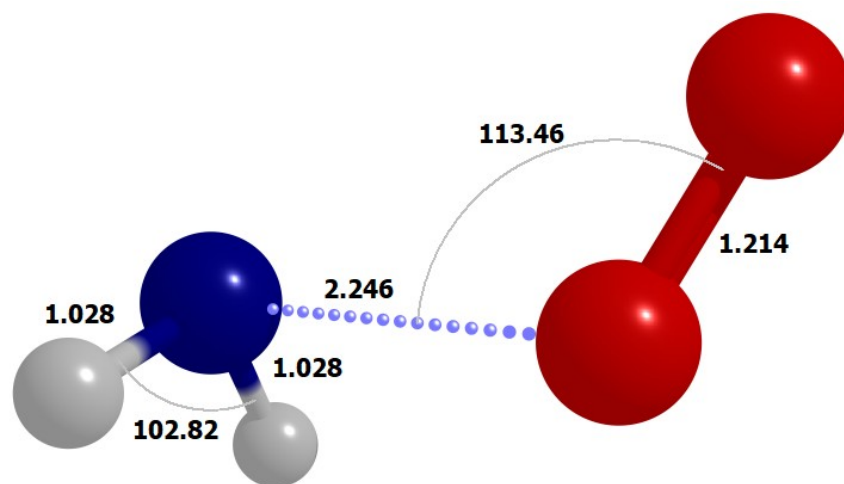


Fig. S15:  $\text{H}_2\text{N}\dots\text{O}_2$  complex, NEVPT2(13e,11o)/aug-cc-pVTZ, bond lengths in the units of Ångström.



Vibrational frequencies, from int. coord. ( $\text{cm}^{-1}$ ):

$$\tilde{\nu}_1 = 105.72i, \tilde{\nu}_2 = 51.90, \tilde{\nu}_3 = 243.72, \tilde{\nu}_4 = 477.65, \tilde{\nu}_5 = 629.40, \tilde{\nu}_6 = 1522.28, \tilde{\nu}_7 = 1541.92, \\ \tilde{\nu}_8 = 3346.32, \tilde{\nu}_9 = 3429.12$$

Rotational constants ( $\text{cm}^{-1}$ ): 1.90828, 0.220325, 0.203740

Fig. S16:  $\text{H}_2\text{N} \cdots \text{O}_2$  PES saddle point, NEVPT2(13e,11o)/aug-cc-pVTZ, bond lengths in the units of Ångström.

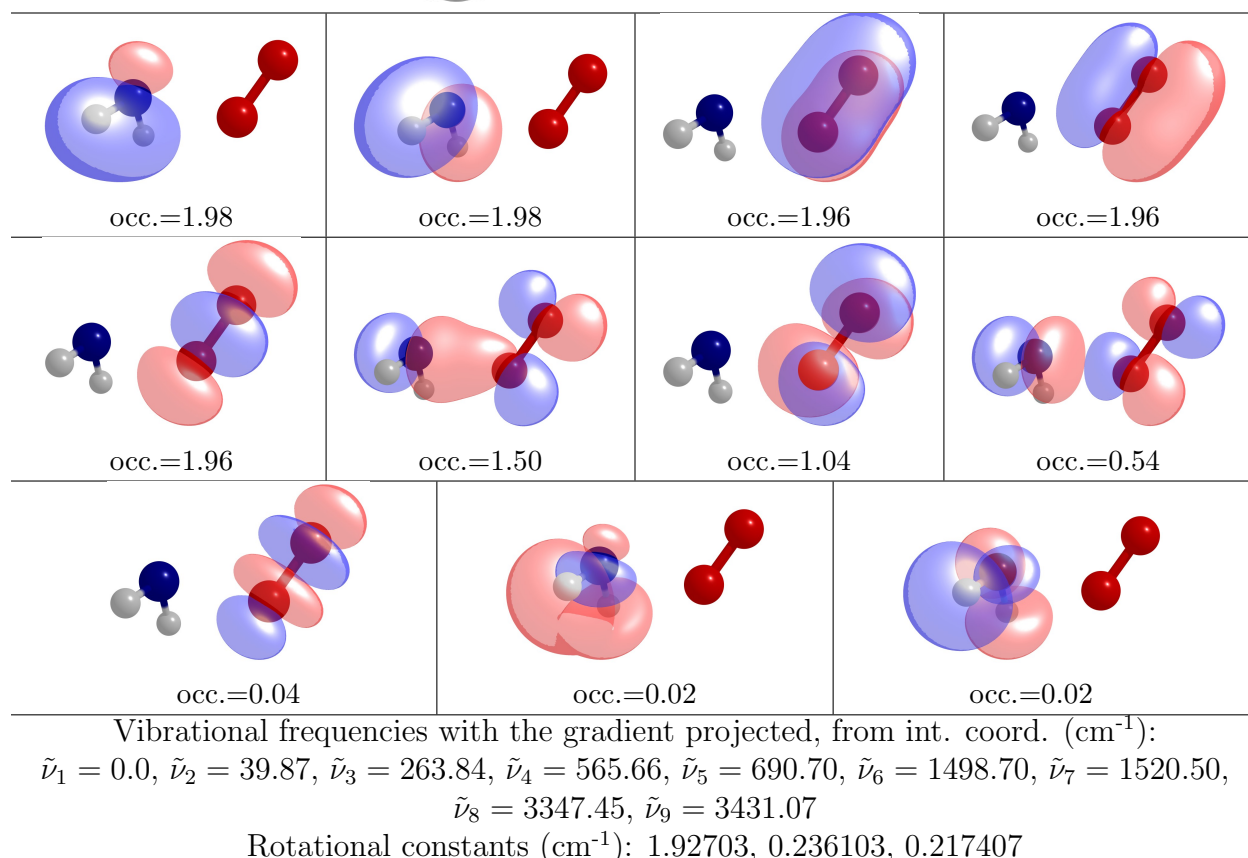
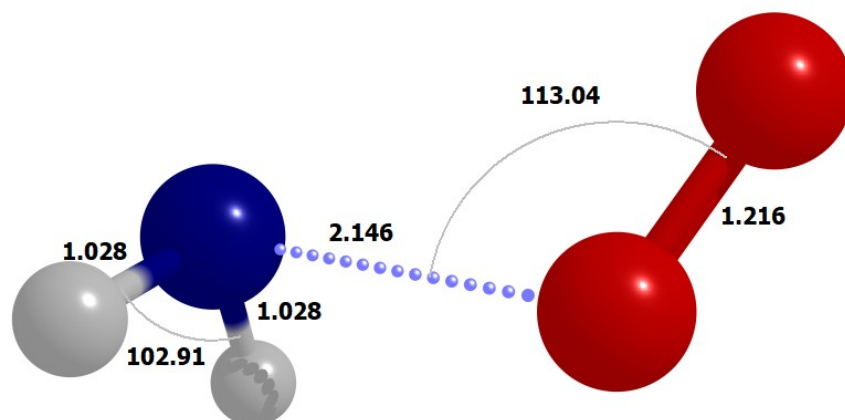
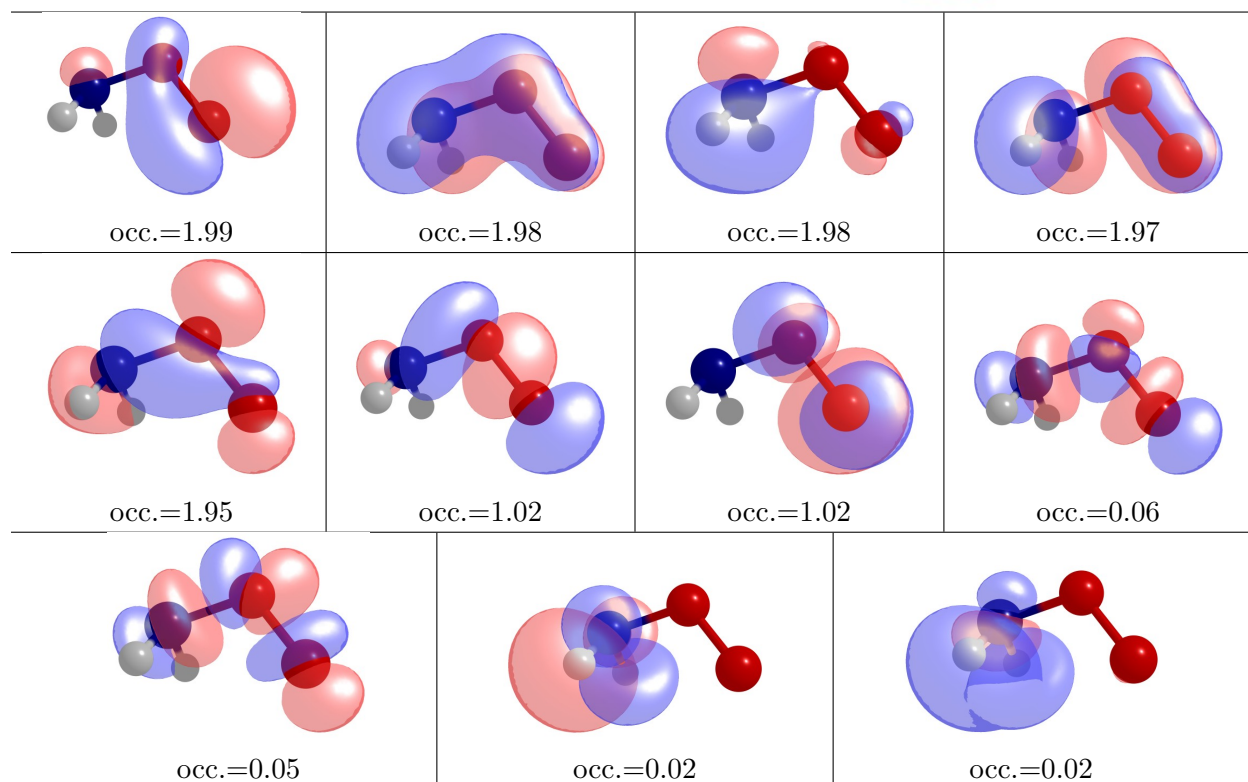
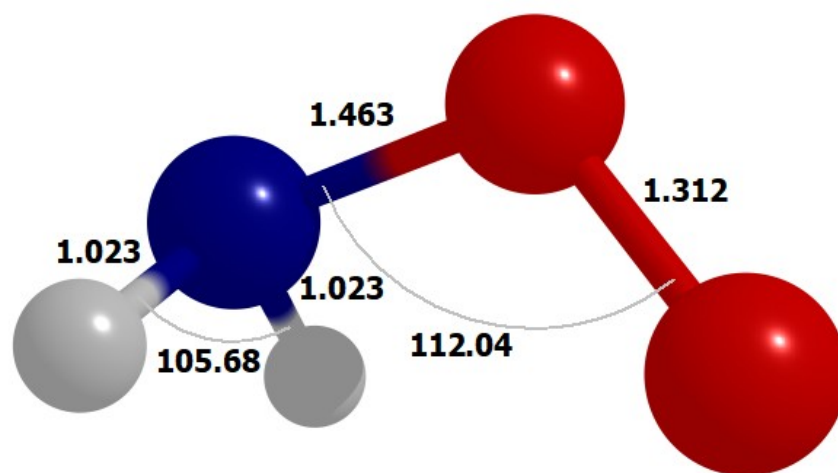


Fig. S17:  $\text{H}_2\text{N}\cdots\text{O}_2$  CVT transition state structure, NEVPT2(13e,11o)/aug-cc-pVTZ, bond lengths in the units of Ångström.



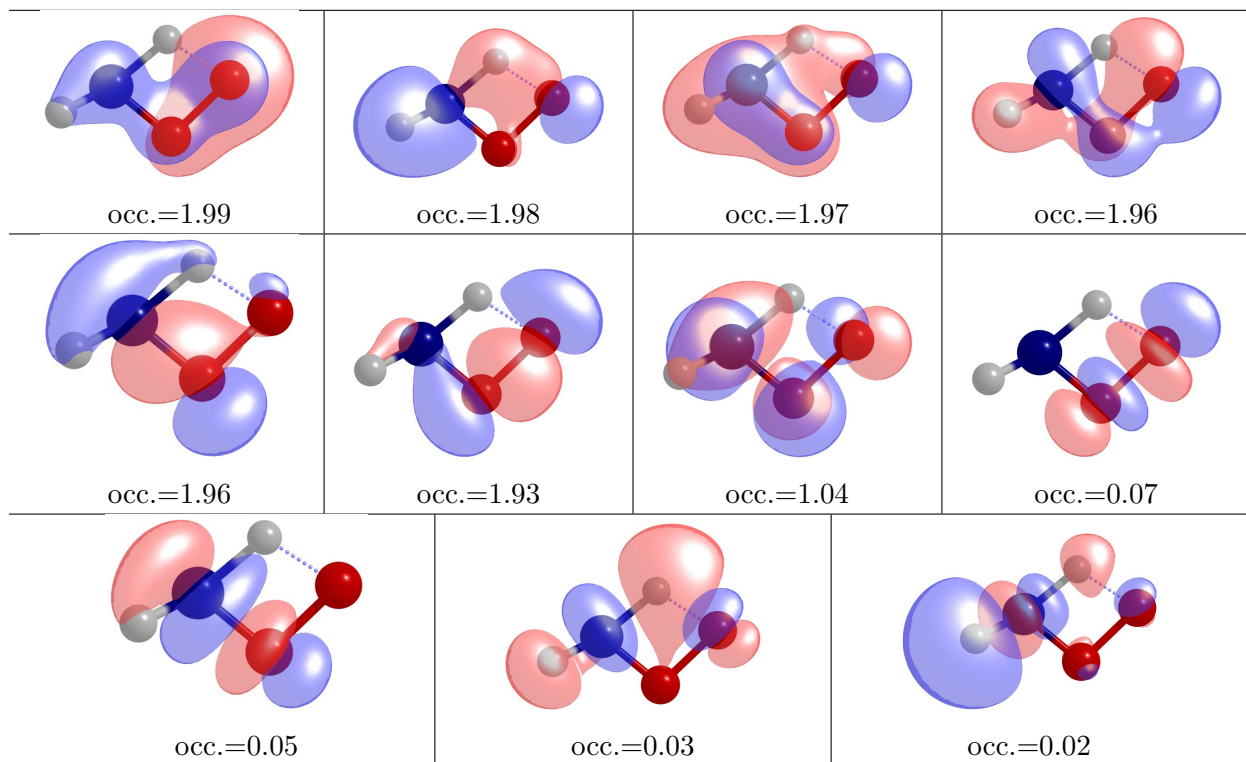
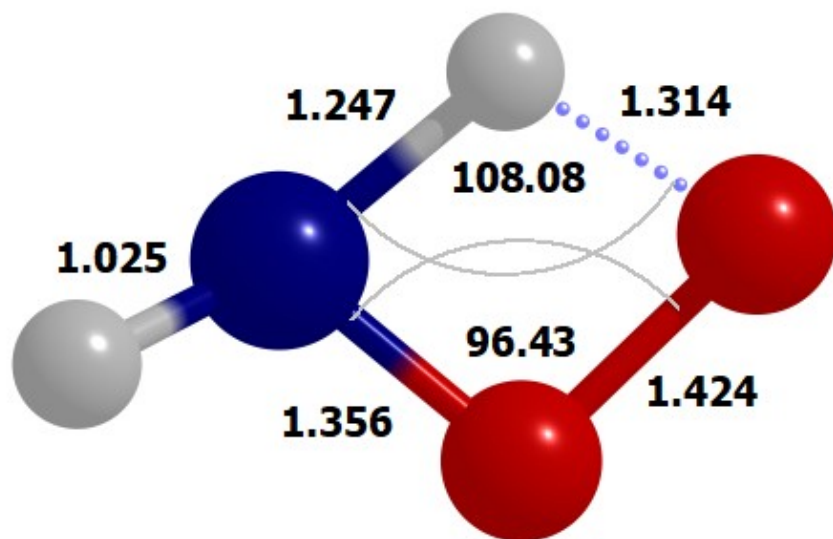
Vibrational frequencies, from int. coord. ( $\text{cm}^{-1}$ ):

$$\tilde{\nu}_1 = 113.95, \tilde{\nu}_2 = 494.09, \tilde{\nu}_3 = 610.85, \tilde{\nu}_4 = 1045.02, \tilde{\nu}_5 = 1220.92, \tilde{\nu}_6 = 1289.69,$$

$$\tilde{\nu}_7 = 1602.59, \tilde{\nu}_8 = 3391.61, \tilde{\nu}_9 = 3477.22$$

Rotational constants ( $\text{cm}^{-1}$ ): 1.88633, 0.387634, 0.338873

Fig. S18:  $\text{NH}_2\text{O}_2$ , NEVPT2(13e,11o)/aug-cc-pVTZ, bond lengths in the units of Ångström.



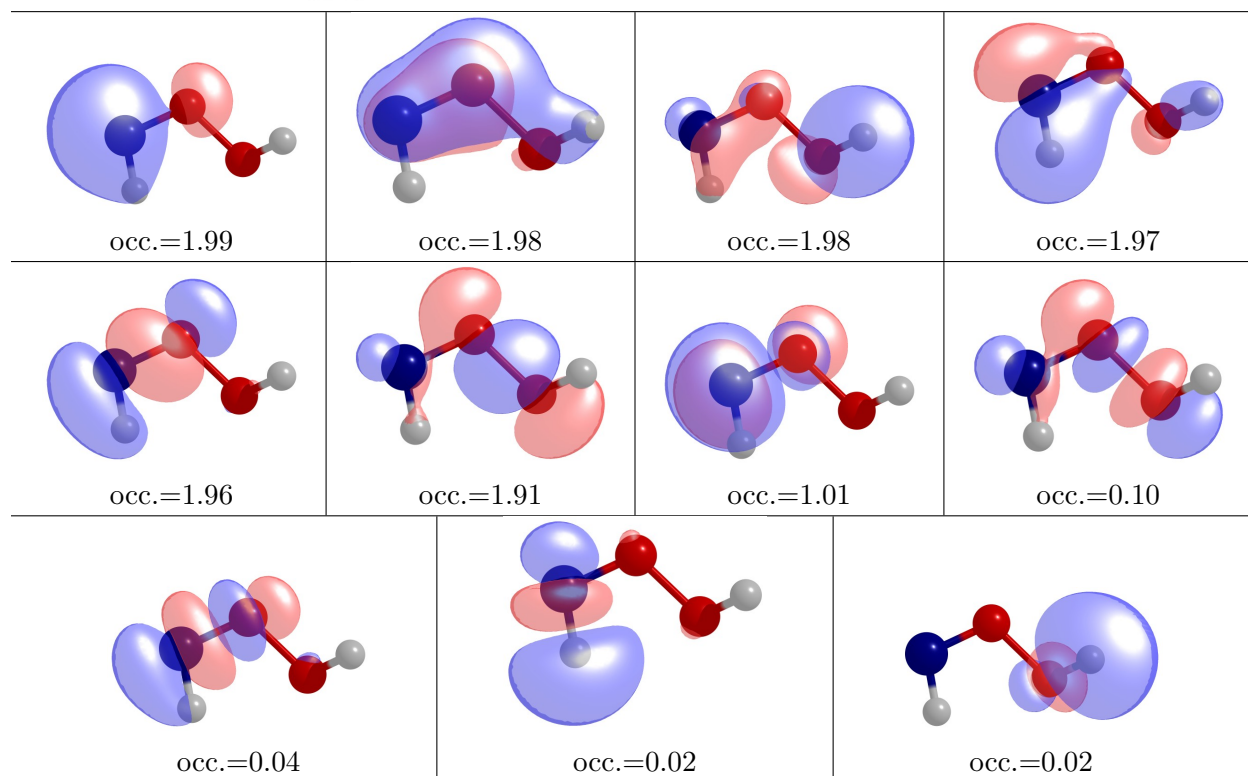
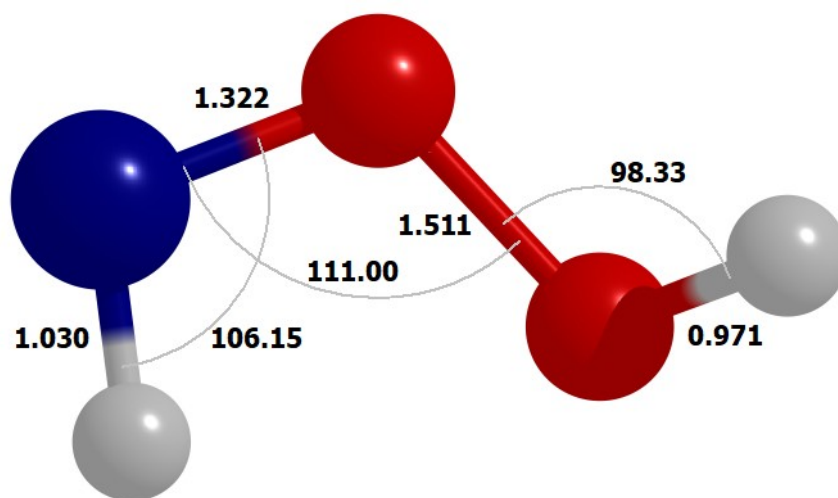
Vibrational frequencies, from Cart. coord. ( $\text{cm}^{-1}$ ):

$$\tilde{\nu}_1 = 1951.57i, \tilde{\nu}_2 = 492.93, \tilde{\nu}_3 = 636.32, \tilde{\nu}_4 = 895.42, \tilde{\nu}_5 = 973.41, \tilde{\nu}_6 = 1074.5,$$

$$\tilde{\nu}_7 = 1367.21, \tilde{\nu}_8 = 2222.95, \tilde{\nu}_9 = 3414.02$$

Rotational constants ( $\text{cm}^{-1}$ ): 1.63475, 0.468341, 0.368689

Fig. S19:  $\text{NH}_2\text{O}_2$  to  $\text{HNOOH}$  isomerization transition state, NEVPT2(13e,11o)/aug-cc-pVTZ, bond lengths in the units of Ångström.



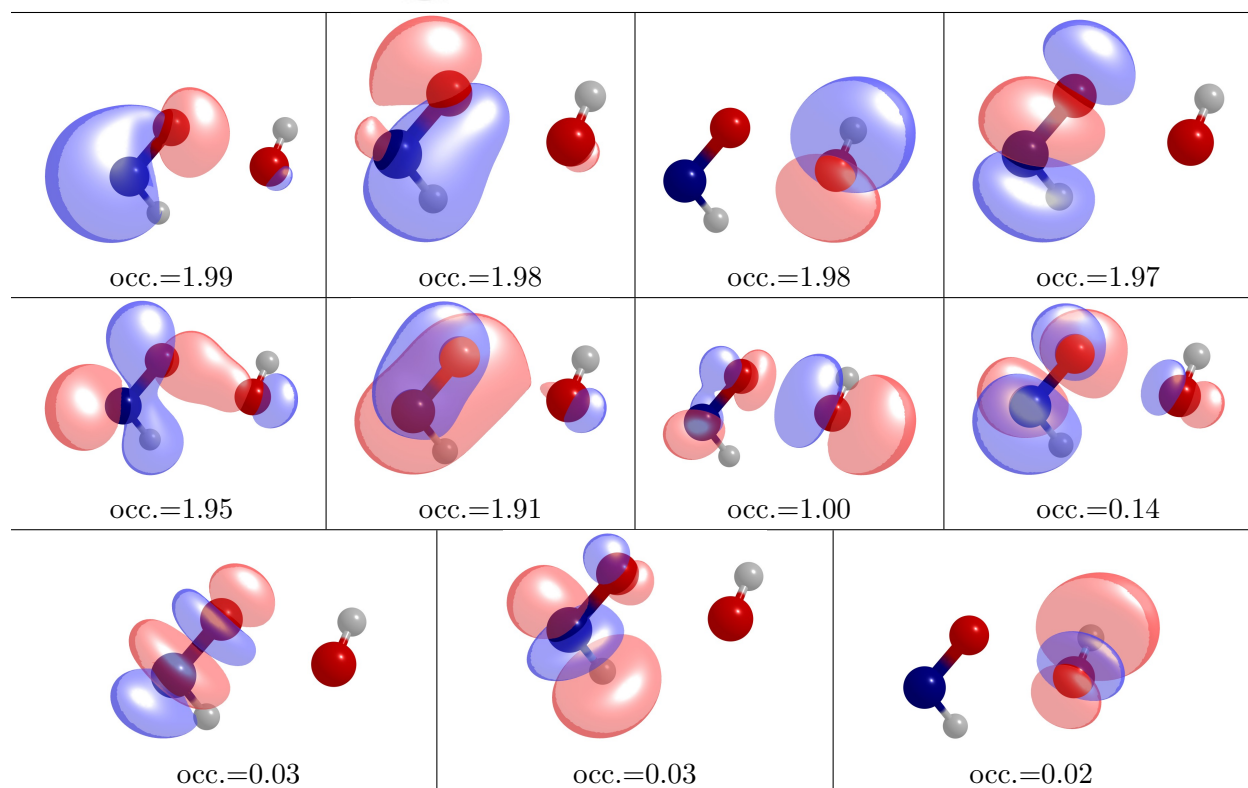
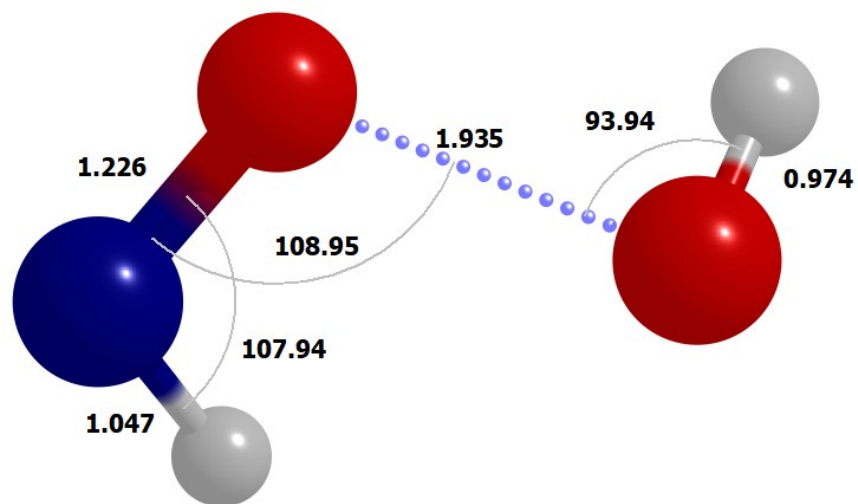
Vibrational frequencies, from Cart. coord. ( $\text{cm}^{-1}$ ):

$$\tilde{\nu}_1 = 175.77, \tilde{\nu}_2 = 327.62, \tilde{\nu}_3 = 485.5, \tilde{\nu}_4 = 706.28, \tilde{\nu}_5 = 1059.38, \tilde{\nu}_6 = 1266.49,$$

$$\tilde{\nu}_7 = 1426.04, \tilde{\nu}_8 = 3364.33, \tilde{\nu}_9 = 3731.43$$

Rotational constants ( $\text{cm}^{-1}$ ): 1.92045, 0.375223, 0.321175

Fig. S20: HNOOH, NEVPT2(13e,11o)/aug-cc-pVTZ, bond lengths in the units of Ångström.



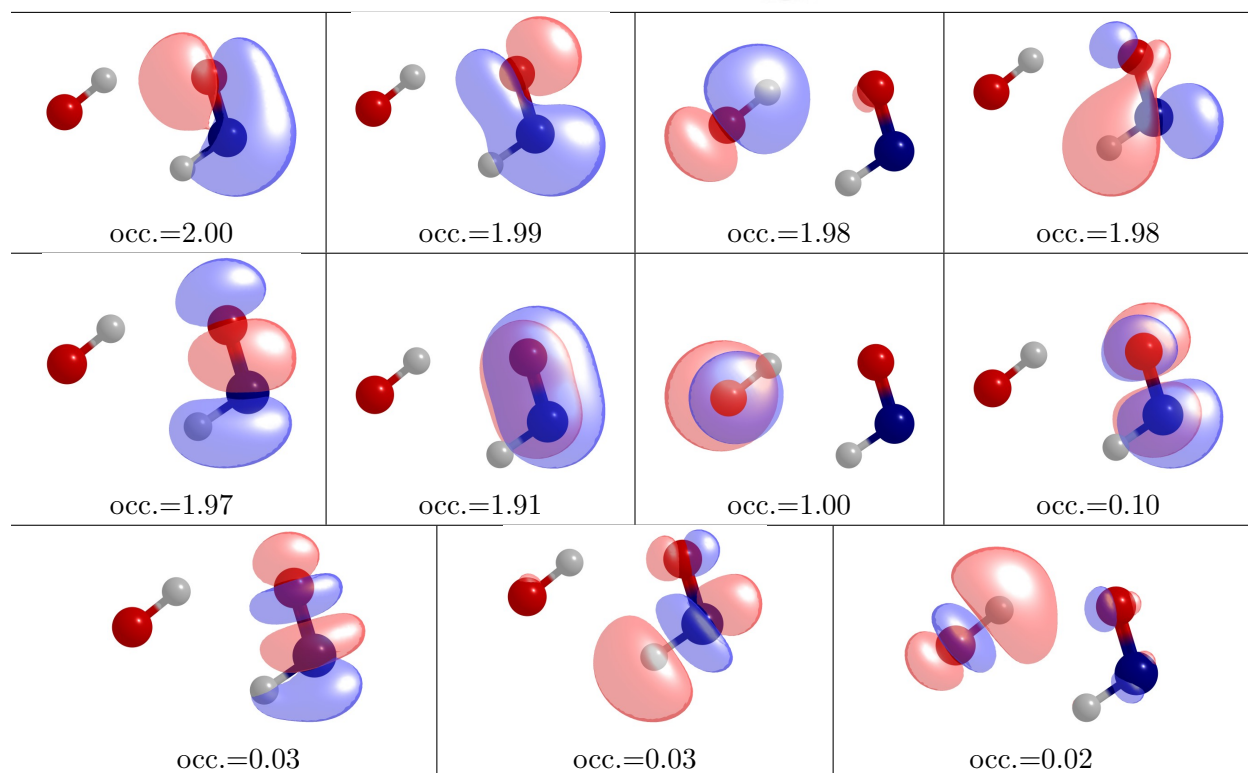
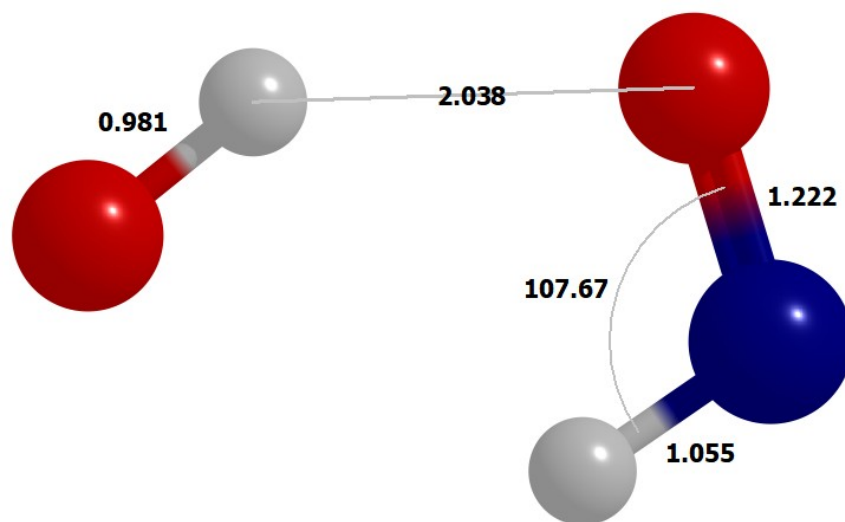
Vibrational frequencies, from Cart. coord. ( $\text{cm}^{-1}$ ):

$$\tilde{\nu}_1 = 664.22i, \tilde{\nu}_2 = 186.86, \tilde{\nu}_3 = 265.62, \tilde{\nu}_4 = 652.52, \tilde{\nu}_5 = 789.80, \tilde{\nu}_6 = 1427.97,$$

$$\tilde{\nu}_7 = 1472.99, \tilde{\nu}_8 = 3062.82, \tilde{\nu}_9 = 3727.29$$

Rotational constants ( $\text{cm}^{-1}$ ): 1.77061, 0.288838, 0.252530

Fig. S21: HNO  $\cdots$  OH transition state, NEVPT2(13e,11o)/aug-cc-pVTZ, bond lengths in the units of Ångström.



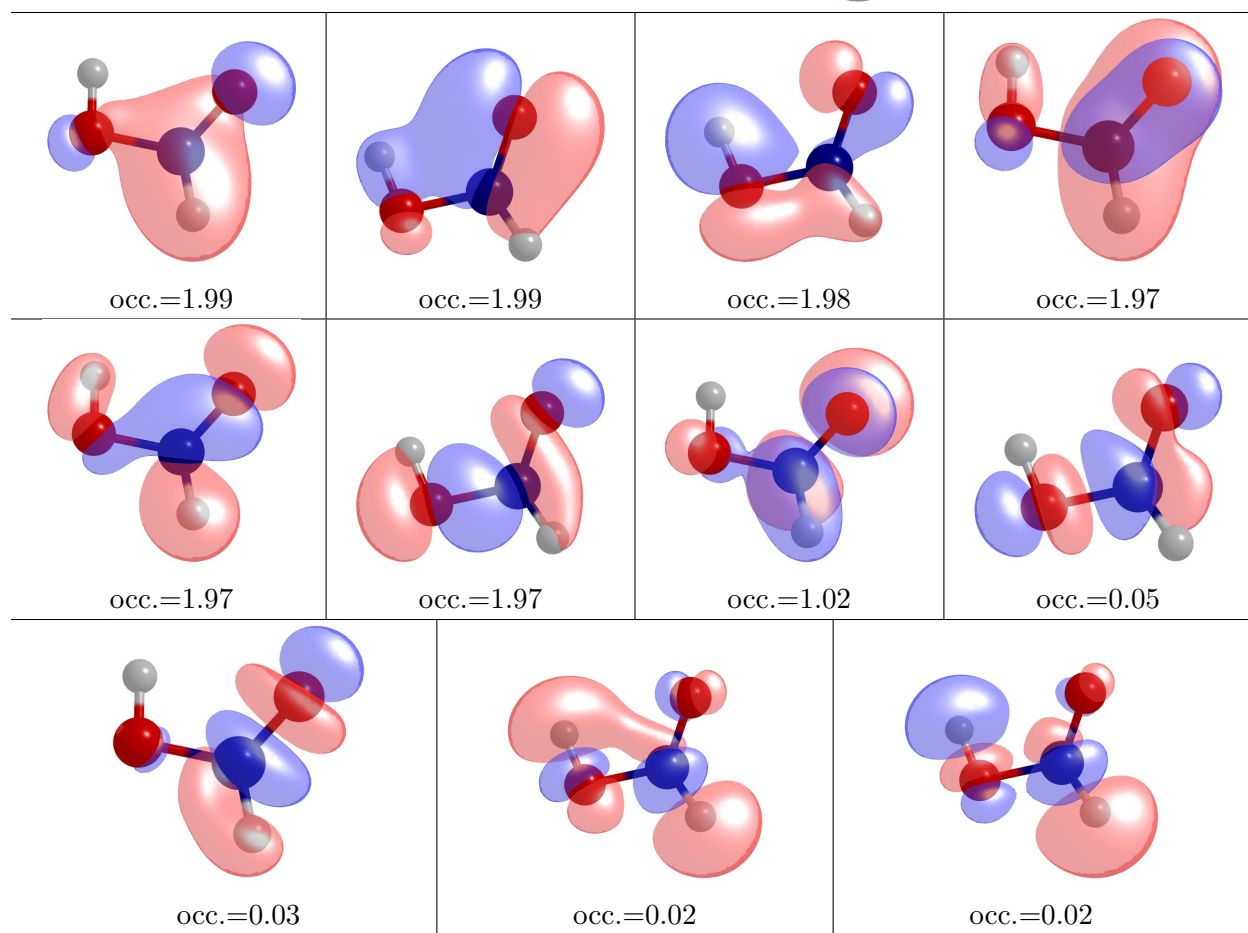
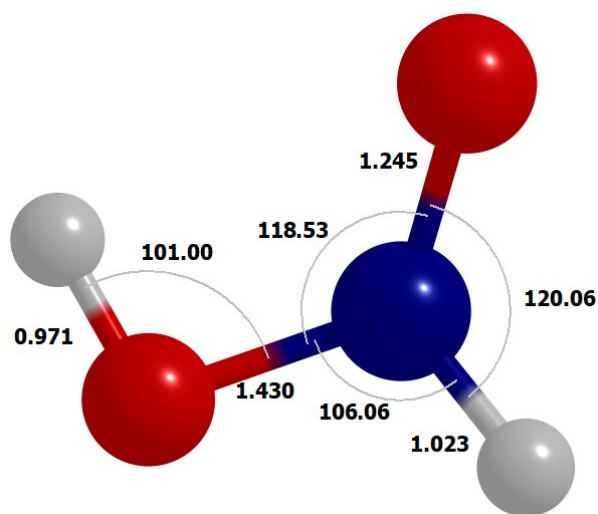
Vibrational frequencies, from Cart. coord. ( $\text{cm}^{-1}$ ):

$$\tilde{\nu}_1 = 112.64, \tilde{\nu}_2 = 186.51, \tilde{\nu}_3 = 272.39, \tilde{\nu}_4 = 403.64, \tilde{\nu}_5 = 467.24, \tilde{\nu}_6 = 1525.24,$$

$$\tilde{\nu}_7 = 1591.98, \tilde{\nu}_8 = 2994.96, \tilde{\nu}_9 = 3626.17$$

Rotational constants ( $\text{cm}^{-1}$ ): 1.39759 , 0.178852, 0.158561

Fig. S22: HNO...OH complex, NEVPT2(13e,11o)/aug-cc-pVTZ, bond lengths in the units of Ångström.

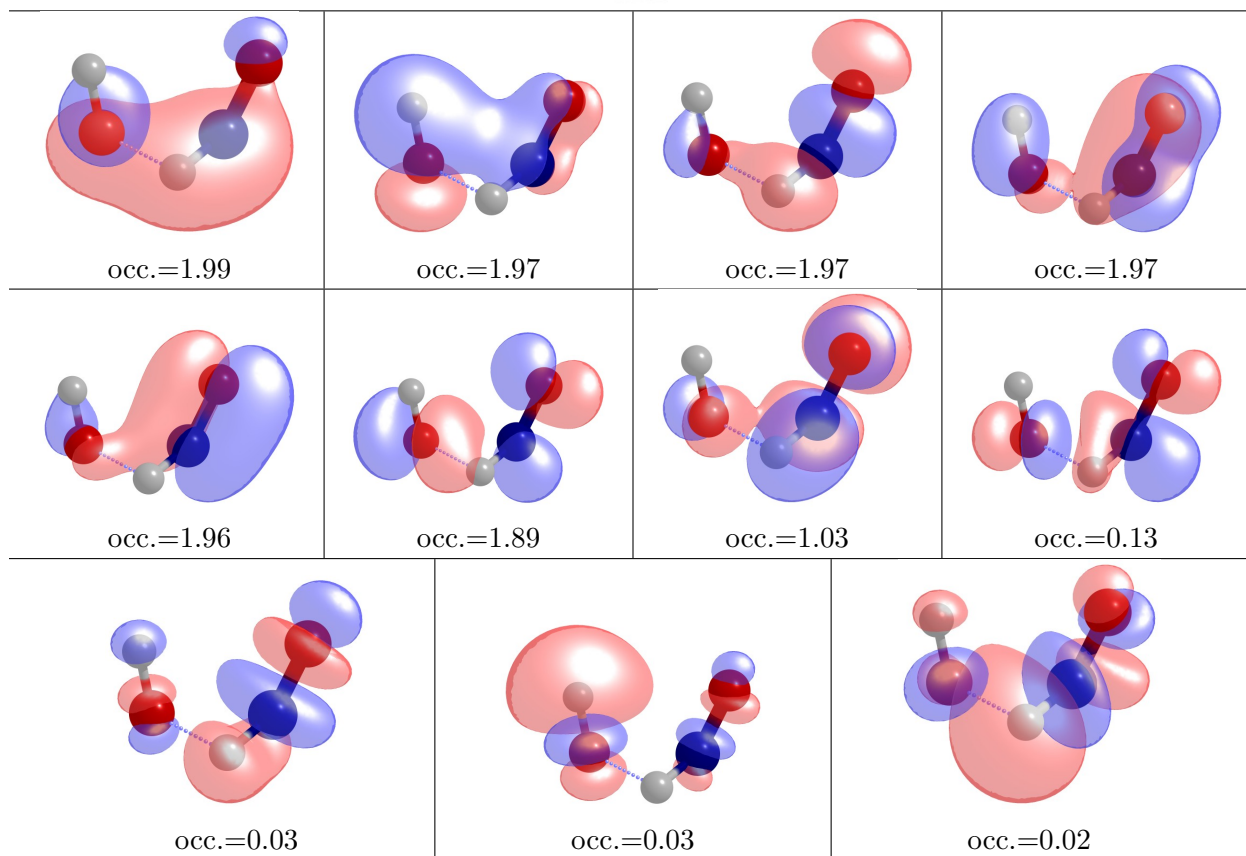
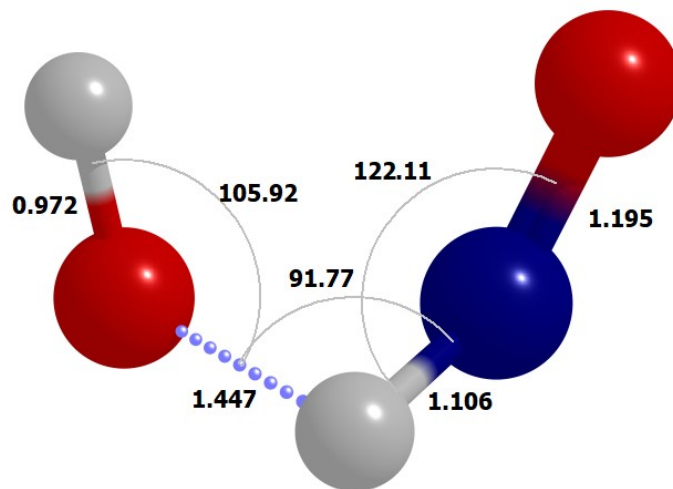


Vibrational frequencies ( $\text{cm}^{-1}$ ):

$$\tilde{\nu}_1 = 220.95, \tilde{\nu}_2 = 542.65, \tilde{\nu}_3 = 765.75, \tilde{\nu}_4 = 935.17, \tilde{\nu}_5 = 1295.98, \tilde{\nu}_6 = 1414.67, \\ \tilde{\nu}_7 = 1518.64, \tilde{\nu}_8 = 3403.5, \tilde{\nu}_9 = 3718.27$$

Rotational constants ( $\text{cm}^{-1}$ ): 2.18457, 0.384933, 0.332034

Fig. S23: HONHO, NEVPT2(13e,11o)/aug-cc-pVTZ, bond lengths in the units of Ångström.



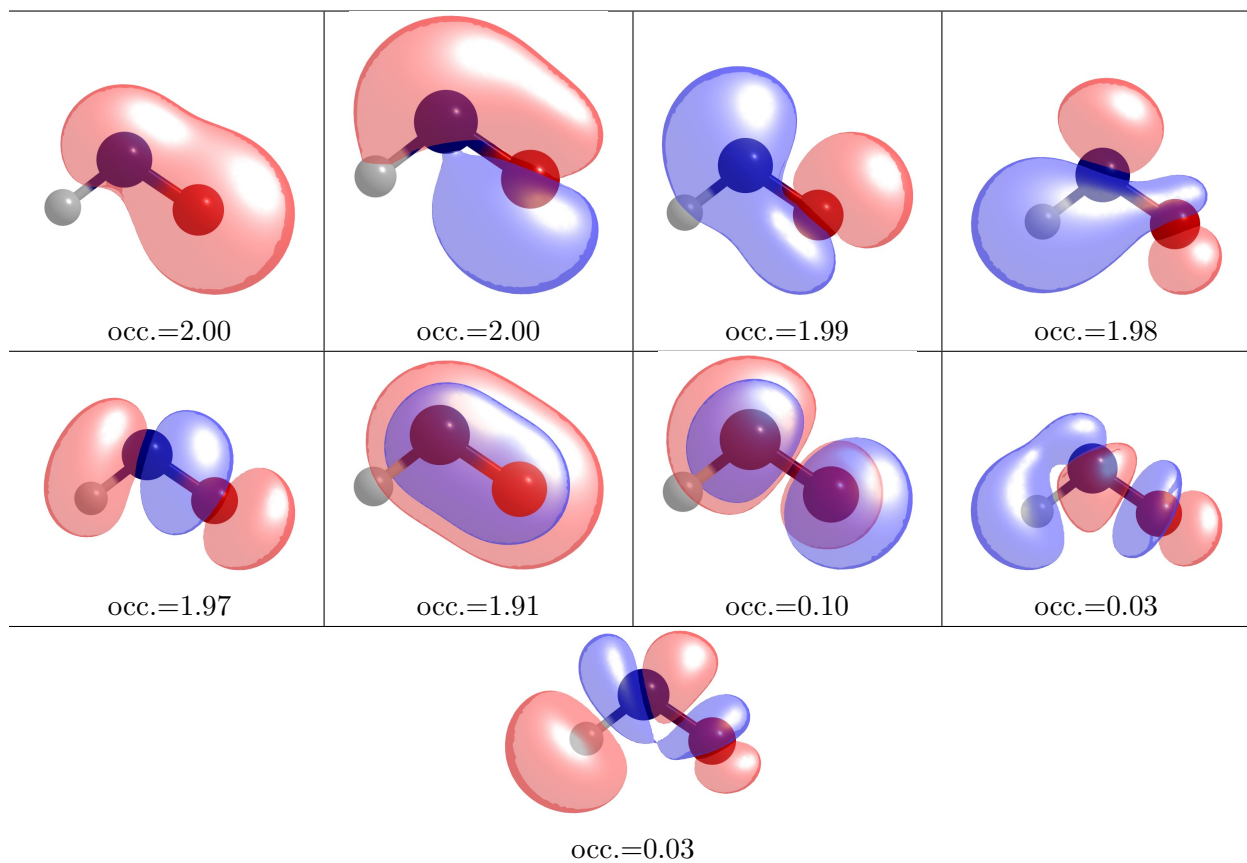
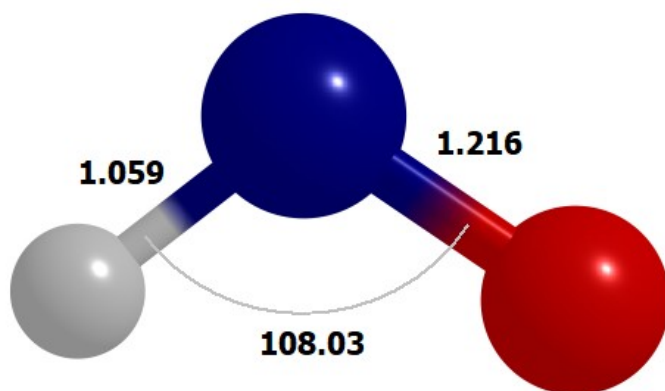
Vibrational frequencies, from Cart. coord. ( $\text{cm}^{-1}$ ):

$$\tilde{\nu}_1 = 1746.35i, \tilde{\nu}_2 = 333.31, \tilde{\nu}_3 = 386.67, \tilde{\nu}_4 = 562.12, \tilde{\nu}_5 = 863.26, \tilde{\nu}_6 = 1094.43,$$

$$\tilde{\nu}_7 = 1603.71, \tilde{\nu}_8 = 2273.54, \tilde{\nu}_9 = 3716.03$$

Rotational constants ( $\text{cm}^{-1}$ ): 2.12621, 0.295305, 0.264312

Fig. S24: HO  $\cdots$  H-NO transition state, NEVPT2(13e,11o)/aug-cc-pVTZ, bond lengths in the units of Ångström.

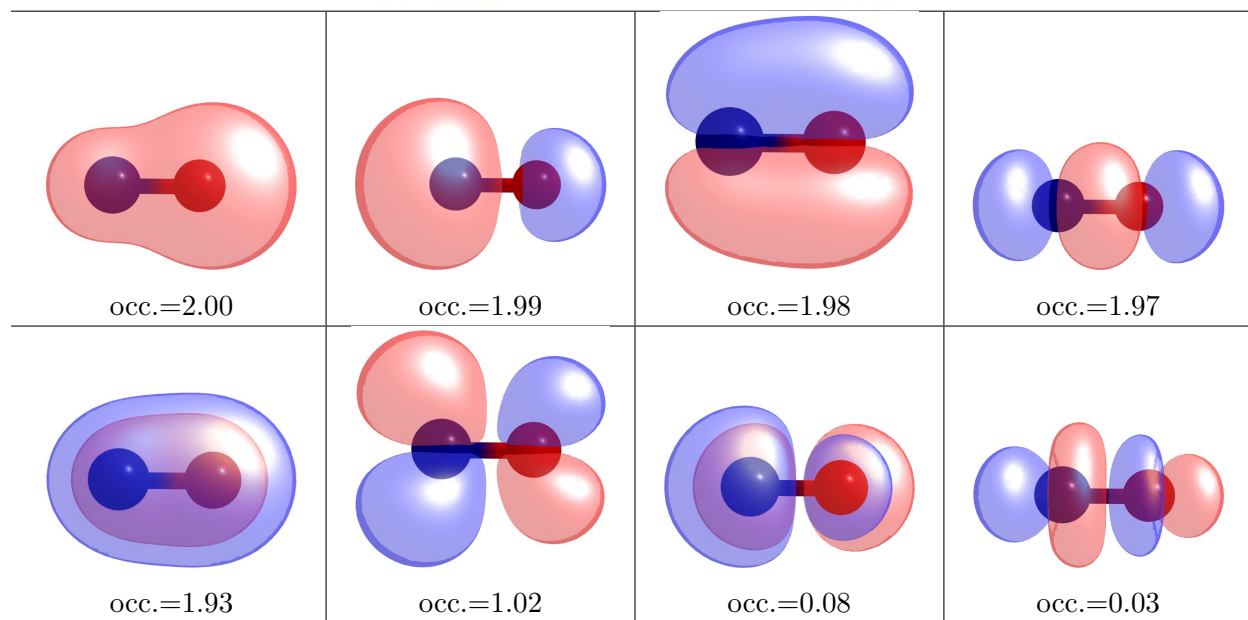
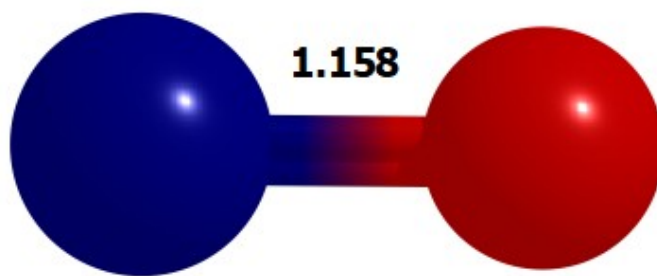


Vibrational frequencies, from int. coord. ( $\text{cm}^{-1}$ ):

$$\tilde{\nu}_1 = 1532.84, \tilde{\nu}_2 = 1584.93, \tilde{\nu}_3 = 2906.46$$

Rotational constants ( $\text{cm}^{-1}$ ): 18.5927, 1.39933, 1.301389

Fig. S25: HNO ( $C_s$ ), NEVPT2(12e,9o)/aug-cc-pVTZ, bond lengths in the units of Ångström.

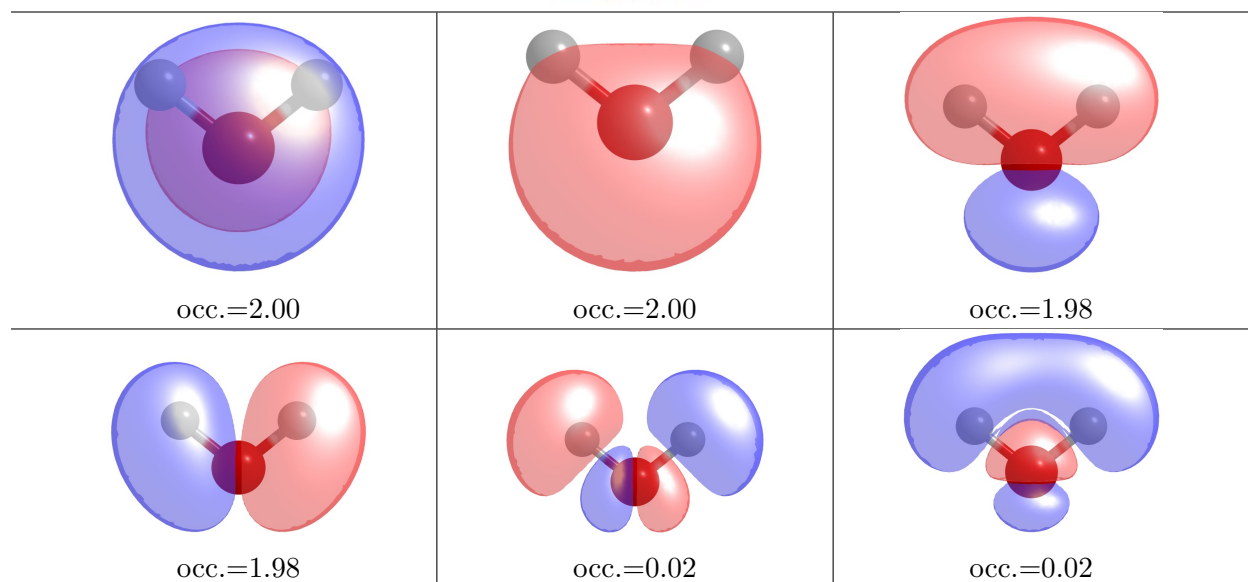
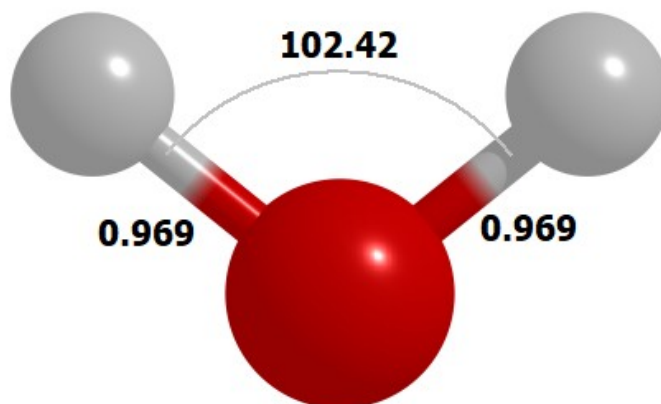


Vibrational frequency ( $\text{cm}^{-1}$ ):

$$\tilde{\nu}_1 = 1876.60$$

Rotational constants ( $\text{cm}^{-1}$ ): 0.00000, 1.68246, 1.68246

Fig. S26: NO ( $C_{\infty v}$ ), NEVPT2(11e,8o)/aug-cc-pVTZ, bond lengths in the units of Ångström.



Vibrational frequencies, from int. coord. ( $\text{cm}^{-1}$ ):

$$\tilde{\nu}_1 = 1691.11, \tilde{\nu}_2 = 3783.09, \tilde{\nu}_3 = 3798.42$$

Rotational constants ( $\text{cm}^{-1}$ ): 25.5468, 14.6576, 9.31376

Fig. S27:  $\text{H}_2\text{O}$  ( $\text{C}_{2v}$ ), NEVPT2(8e,6o)/aug-cc-pVTZ, bond lengths in the units of Ångström.

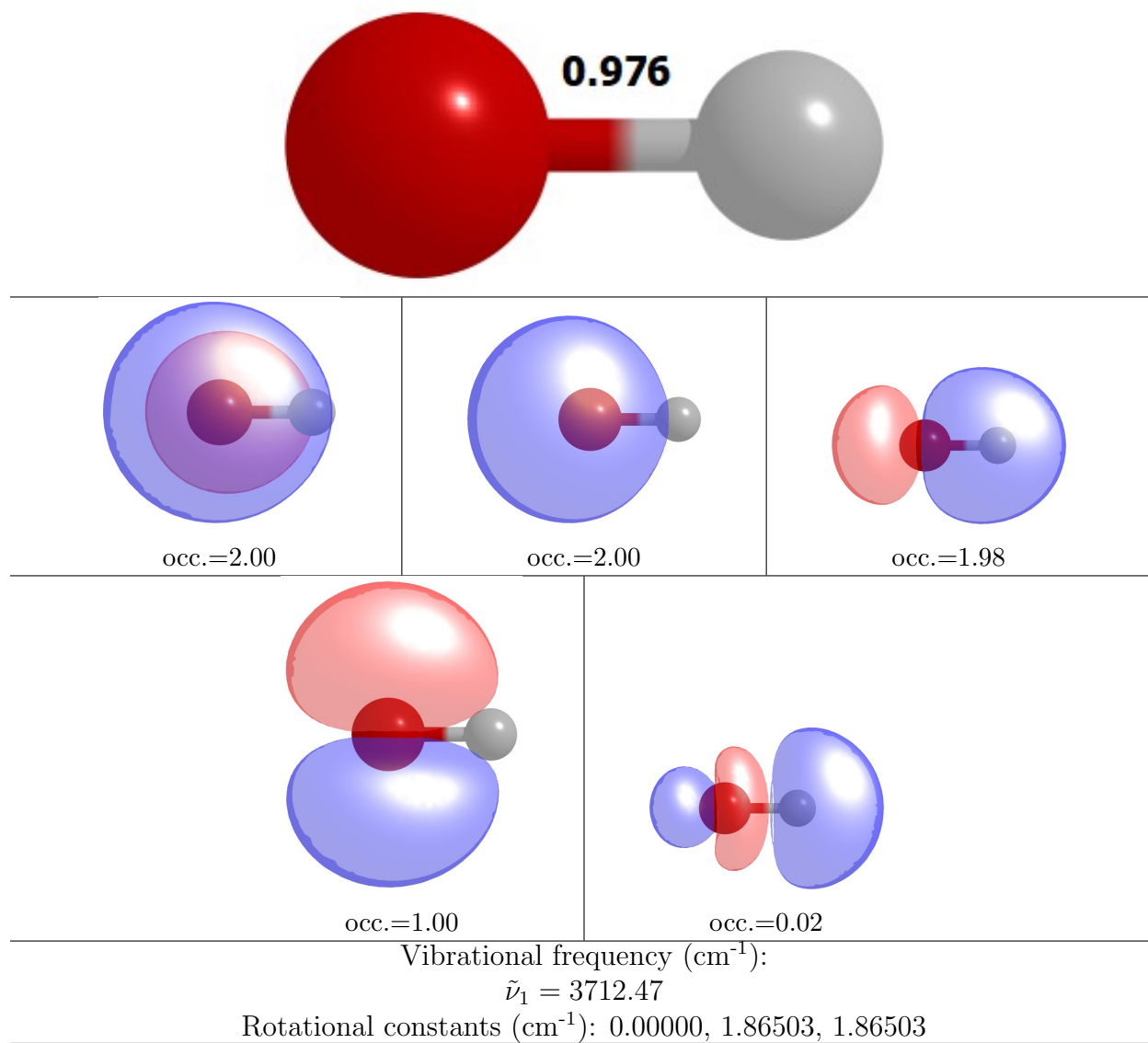
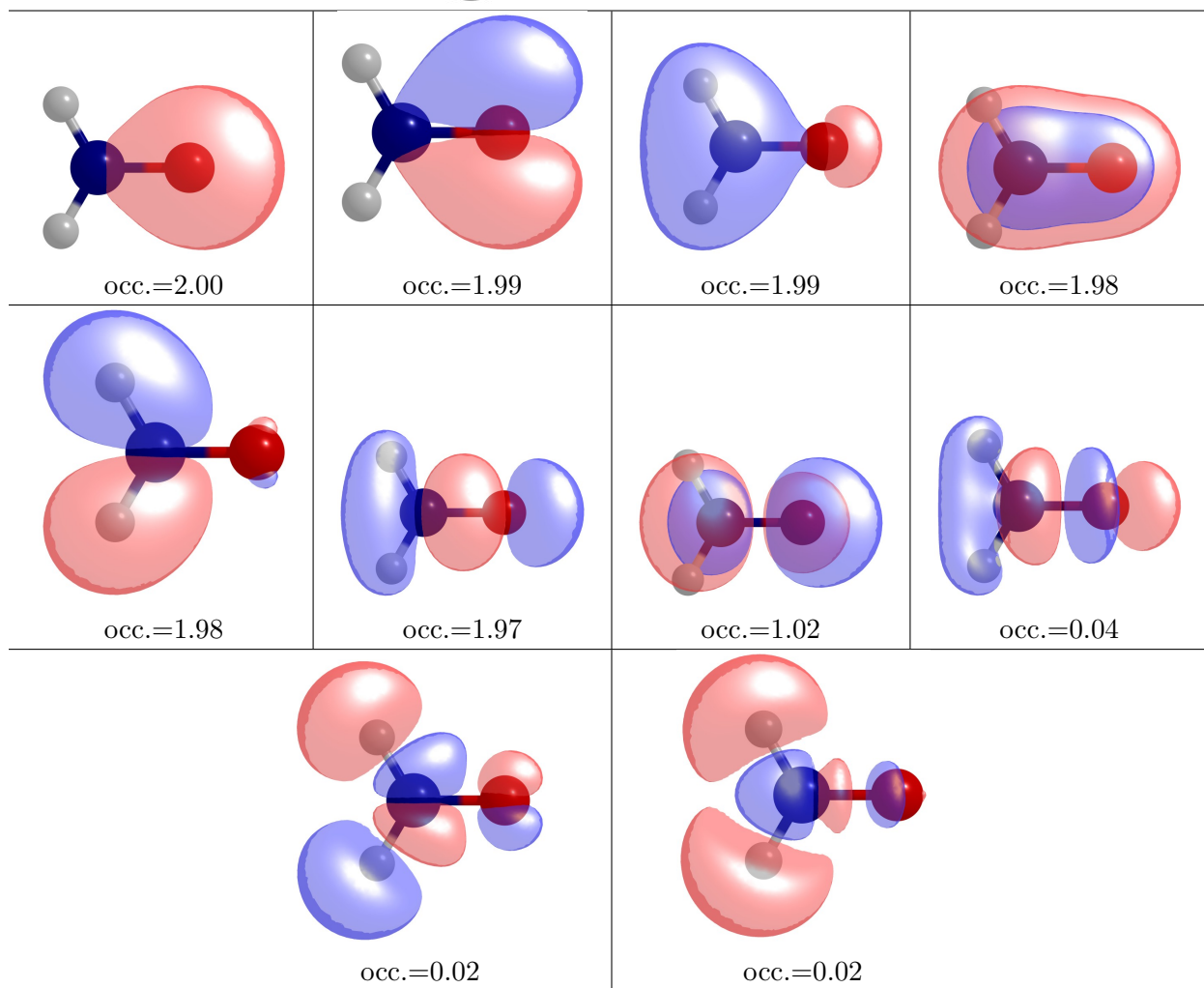
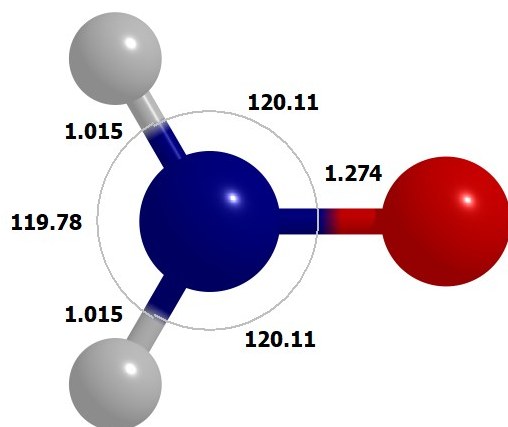


Fig. S28: OH ( $C_{\infty v}$ ), NEVPT2(7e,5o)/aug-cc-pVTZ, bond lengths in the units of Ångström.



Vibrational frequencies, from Cart. coord. ( $\text{cm}^{-1}$ ):

$\tilde{\nu}_1 = 206.76$ ,  $\tilde{\nu}_1 = 1258.66$ ,  $\tilde{\nu}_1 = 1396.37$ ,  $\tilde{\nu}_1 = 1683.10$ ,  $\tilde{\nu}_1 = 3449.10$ ,  $\tilde{\nu}_1 = 3571.31$

Rotational constants ( $\text{cm}^{-1}$ ): 10.8480, 1.14057, 1.03206

Fig. S29:  $\text{NH}_2\text{O}$  ( $C_s$ ), NEVPT2(13e,10o)/aug-cc-pVTZ, bond lengths in the units of Ångström.

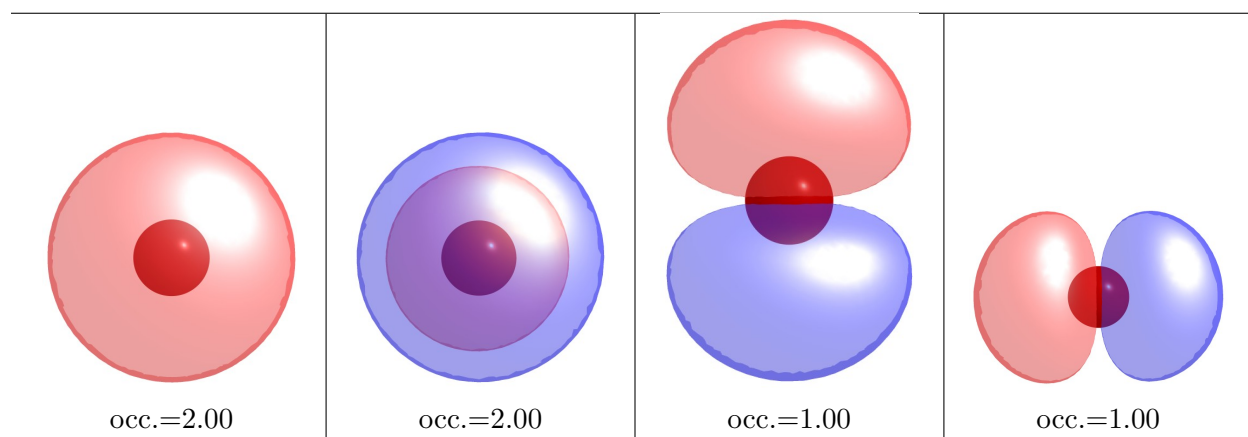


Fig. S30:  $O(^3P)$ , NEVPT2(6e,4o)/aug-cc-pVTZ.

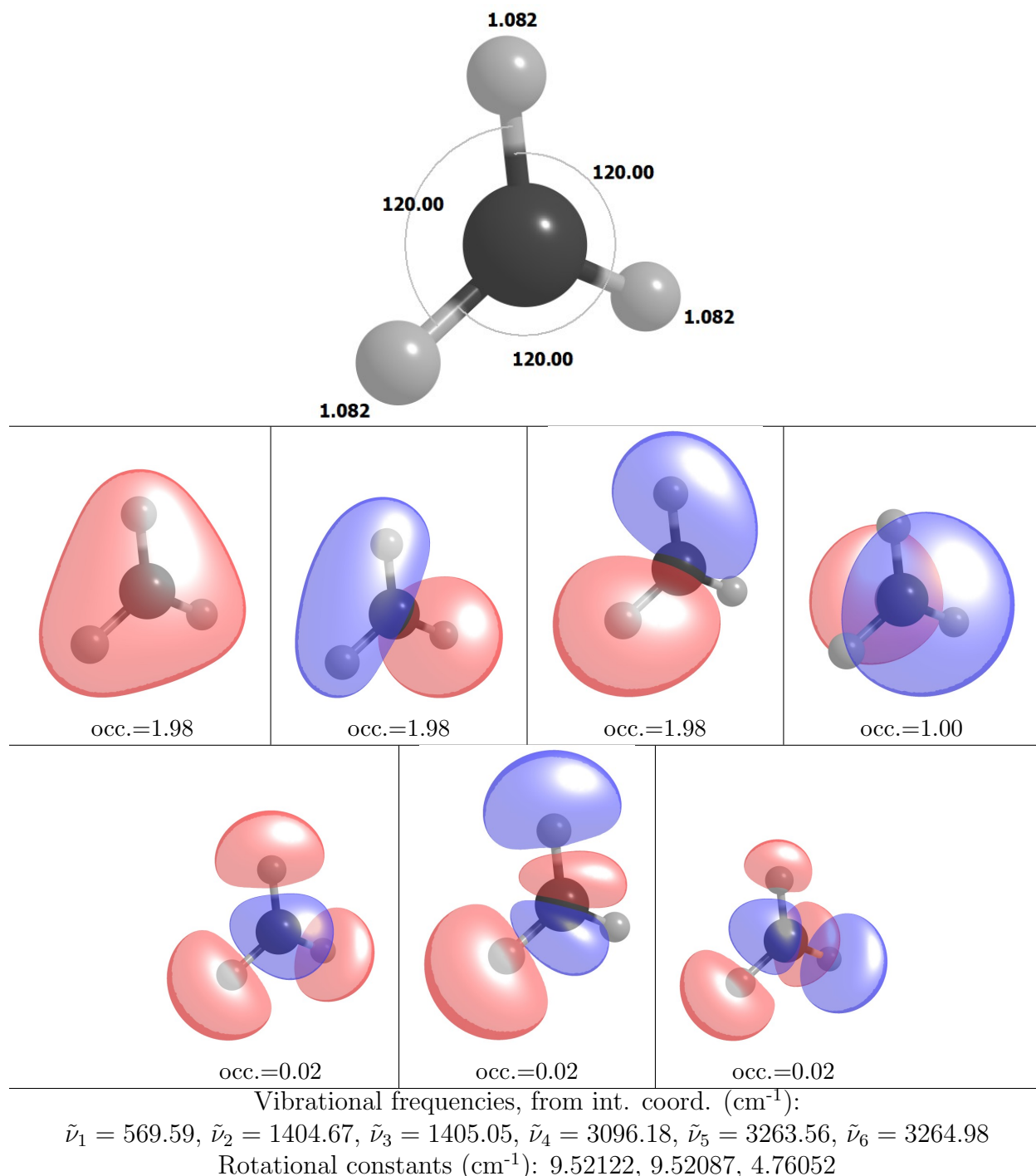


Fig. S31:  $\text{CH}_3$  ( $D_{3h}$ ), NEVPT2(7e,7o)/aug-cc-pVTZ, bond lengths in the units of Ångström.

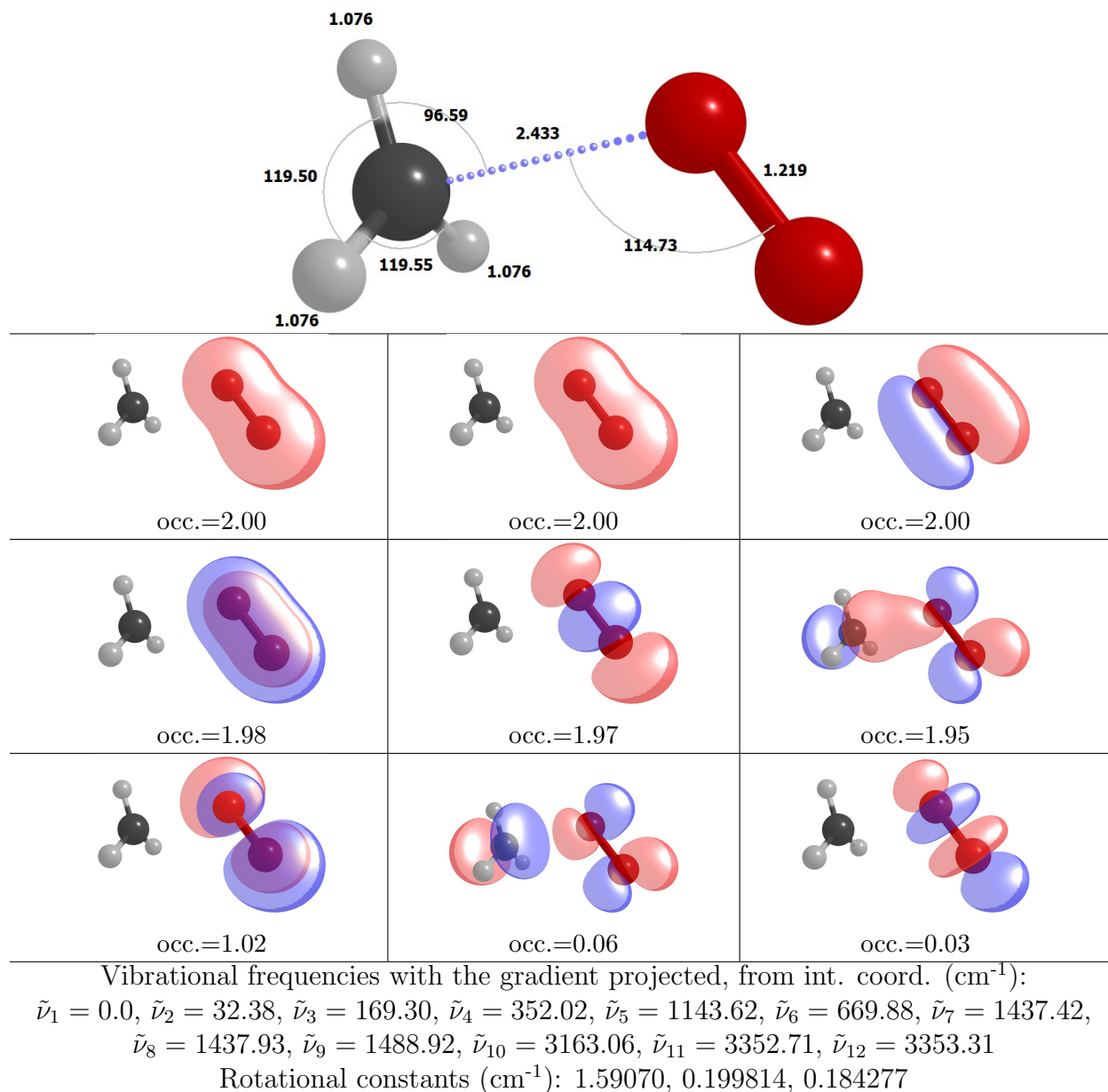
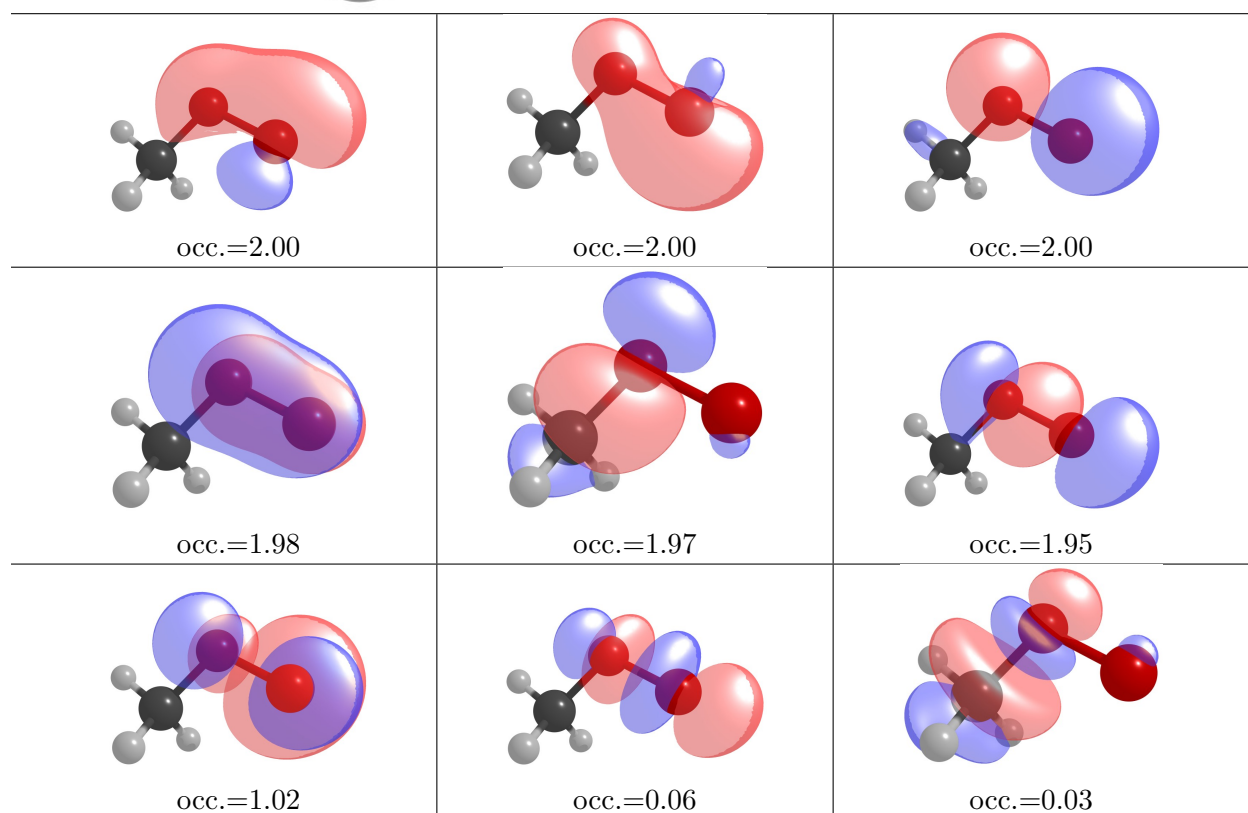
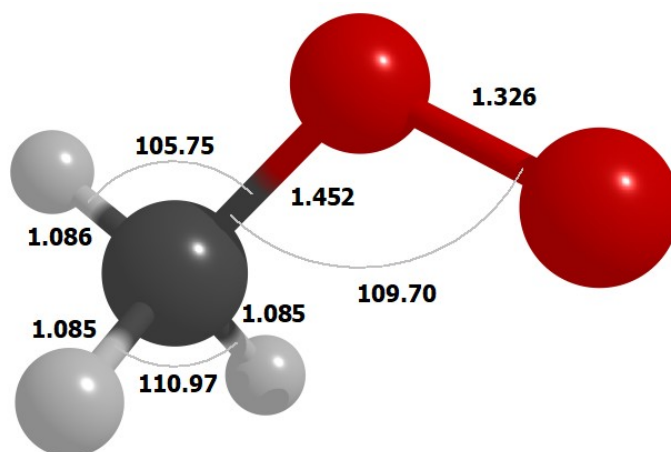


Fig. S32:  $\text{H}_3\text{C}\cdots\text{O}_2$  CVT transition state structure, NEVPT2(13e,9o)/aug-cc-pVTZ, bond lengths in the units of Ångström.



Vibrational frequencies, from int. coord. ( $\text{cm}^{-1}$ ):

$\tilde{\nu}_1 = 148.29$ ,  $\tilde{\nu}_2 = 492.42$ ,  $\tilde{\nu}_3 = 934.58$ ,  $\tilde{\nu}_4 = 1138.44$ ,  $\tilde{\nu}_5 = 1143.62$ ,  $\tilde{\nu}_6 = 1216.54$ ,  
 $\tilde{\nu}_7 = 1463.52$ ,  $\tilde{\nu}_8 = 1489.55$ ,  $\tilde{\nu}_9 = 1507.37$ ,  $\tilde{\nu}_{10} = 3103.08$ ,  $\tilde{\nu}_{11} = 3214.83$ ,  $\tilde{\nu}_{12} = 3219.6$

Rotational constants ( $\text{cm}^{-1}$ ): 1.70791, 0.379869, 0.330392

Fig. S33:  $\text{CH}_3\text{O}_2$ , NEVPT2(13e,9o)/aug-cc-pVTZ, bond lengths in the units of Ångström.

## S9 Geometries of the stationary points at various levels of theory

The subsection titles denote the level of theory with which the geometries have been obtained.

The *xyz*-coordinates are given in units of Ångström.

### S9.1 $\omega$ B97X-D3/aug-cc-pVTZ

<b>O<sub>2</sub></b>			
<b>0 3</b>			
O	-0.789377178583	-1.973558964513	-5.678285093323
O	-1.479866083947	-1.349553682905	-4.929116859693

---

<b>NH<sub>2</sub></b>			
<b>0 2</b>			
N	-0.672113000000	-0.158601000000	-4.674218000000
H	-0.542470000000	0.792919000000	-5.029861000000
H	0.052744000000	-0.245840000000	-3.956120000000

---

<b>NH<sub>2</sub>O<sub>2</sub></b>			
<b>0 2</b>			
N	-0.971628000000	-0.292921000000	-4.606099000000
H	-1.333078000000	0.370857000000	-5.286292000000
H	0.017770000000	-0.432085000000	-4.799986000000
O	-0.711212000000	-2.351596000000	-5.485223000000
O	-1.567603000000	-1.535687000000	-4.989758000000

---

<b>HNO</b>			
<b>0 1</b>			
O	-0.486859000000	0.573662000000	-1.123814000000
N	0.307958000000	0.584195000000	-2.011868000000
H	0.889323000000	-0.295226000000	-1.956280000000

---

<b>NO</b>			
<b>0 2</b>			
N	-1.459392000000	0.000000000000	-4.327294000000
O	-1.448930000000	0.000000000000	-3.187031000000

---

**H<sub>2</sub>O****0 1**

O	-2.187285000000	-2.975650000000	0.423318000000
H	-2.187285000000	-2.215262000000	1.005240000000
H	-2.187285000000	-3.736039000000	1.005239000000

---

**OH****0 2**

O	-1.449189000000	0.874712000000	-2.763755000000
H	-1.202769000000	1.812193000000	-2.812372000000

---

**NH<sub>2</sub>O****0 2**

N	-1.697681000000	-0.146280000000	-1.781383000000
O	-1.697681000000	1.104834000000	-1.586026000000
H	-0.823957000000	-0.655136000000	-1.744486000000
H	-2.571404000000	-0.655136000000	-1.744486000000

---

**CH<sub>3</sub>****0 2**

C	0.071731000000	-0.158591000000	-0.053634000000
H	-0.323288000000	-0.116378000000	-1.056086000000
H	-0.559223000000	-0.476923000000	0.760876000000
H	1.096591000000	0.118455000000	0.135296000000

---

**CH<sub>3</sub>O<sub>2</sub>****0 2**

O	-0.382709000000	1.405128000000	1.728542000000
O	-0.647649000000	1.191309000000	0.473792000000
C	0.001177000000	-0.000421000000	0.001948000000
H	-0.286945000000	-0.100386000000	0.585956000000
H	1.078311000000	0.118903000000	0.099154000000

---

## S9.2 B3LYP(D3BJ)/aug-cc-pVTZ

O<sub>2</sub>

0 3

O -4.353189000000 -15.807921000000 -8.132394000000

O -4.856962000000 -15.287994000000 -7.168141000000

---

NH<sub>2</sub>

0 2

N -0.246636000000 1.245065000000 -4.073074000000

H -0.578724000000 1.899301000000 -4.791940000000

H 0.739512000000 1.100780000000 -4.321514000000

---

NH<sub>2</sub>O<sub>2</sub>

0 2

N -1.029254000000 -0.272793000000 -4.653241000000

H -1.107195000000 0.088653000000 -5.603832000000

H -0.068461000000 -0.146368000000 -4.337664000000

O -1.525665000000 -2.027931000000 -6.024921000000

O -1.128918000000 -1.714058000000 -4.834067000000

---

HNO

0 1

O -0.491470000000 0.576041000000 -1.120602000000

N 0.308117000000 0.585214000000 -2.012854000000

H 0.893775000000 -0.298624000000 -1.958506000000

---

NO

0 2

N -1.459417000000 0.000000000000 -4.329992000000

O -1.448905000000 0.000000000000 -3.184333000000

---

**H<sub>2</sub>O****0 1**

O	-2.187285000000	-2.975650000000	0.421433000000
H	-2.187285000000	-2.211906000000	1.006182000000
H	-2.187285000000	-3.739395000000	1.006181000000

---

**OH****0 2**

O	-2.187285000000	-2.968533000000	0.417869000000
H	-2.187285000000	-3.743157000000	1.010686000000

---

**NH<sub>2</sub>O****0 2**

N	-0.867462000000	-0.428051000000	-4.814130000000
H	-1.189587000000	0.145845000000	-5.586852000000
H	-0.091778000000	-0.099770000000	-4.247809000000
O	-1.185001000000	-1.662590000000	-4.780013000000

---

### S9.3 CASPT2/aug-cc-pVTZ

<b>O<sub>2</sub></b>			
<b>0 3</b>			
O	-4.350756000000	-15.810432000000	-8.137050000000
O	-4.859395000000	-15.285483000000	-7.163485000000

---

<b>NH<sub>2</sub></b>			
<b>0 2</b>			
N	-0.249144000000	1.243120000000	-4.069379000000
H	-0.576182000000	1.899490000000	-4.793324000000
H	0.739478000000	1.102535000000	-4.323825000000

---

<b>NH<sub>2</sub> + O<sub>2</sub></b>			
<b>0 2</b>			
N	4.947741000000	12.054551000000	-0.545794000000
H	4.616879000000	12.704859000000	-1.270500000000
H	5.932768000000	11.907281000000	-0.801937000000
O	-6.659699000000	-14.675405000000	-9.492680000000
O	-7.475204000000	-13.898953000000	-9.036145000000

---

<b>H<sub>2</sub>N ··· O<sub>2</sub> transition state (PES)</b>			
<b>0 2</b>			
N	-0.935739000000	-0.015385000000	-4.490309000000
H	-1.241202000000	0.329024000000	-5.409285000000
H	0.038010000000	-0.301202000000	-4.653350000000
O	-1.150582000000	-2.268279000000	-5.982037000000
O	-1.569980000000	-1.816656000000	-4.918745000000

---

<b>NH<sub>2</sub>O<sub>2</sub></b>			
<b>0 2</b>			
N	-0.991273000000	-0.240709000000	-4.580065000000
H	-1.277661000000	0.258907000000	-5.424859000000
H	0.014806000000	-0.392165000000	-4.680948000000
O	-1.077365000000	-2.105908000000	-5.938228000000
O	-1.528000000000	-1.592624000000	-4.829627000000

---

## S9.4 NEVPT2/aug-cc-pVTZ

**O<sub>2</sub>**

**0 3**

O -4.351710000000 -15.809448000000 -8.135225000000

O -4.858441000000 -15.286467000000 -7.165310000000

---

**NH<sub>2</sub>**

**0 2**

N -0.251729000000 1.241103000000 -4.065555000000

H -0.572272000000 1.898913000000 -4.794302000000

H 0.738152000000 1.105129000000 -4.326671000000

---

**NH<sub>2</sub> ··· O<sub>2</sub> complex**

**0 2**

N -1.055233000000 0.290798000000 -4.626259000000

H -0.606306000000 0.586747000000 -5.503283000000

H -0.253971000000 0.009462000000 -4.045611000000

O -2.003260000000 -2.771683000000 -5.639718000000

O -0.940722000000 -2.187823000000 -5.638855000000

---

**H<sub>2</sub>N ··· O<sub>2</sub> transition state (PES)**

**0 2**

N -0.903303000000 0.094500000000 -4.452122000000

H -1.835502000000 0.294069000000 -4.066202000000

H -1.007207000000 0.349330000000 -5.443097000000

O -0.893886000000 -2.851232000000 -4.557120000000

O -1.621475000000 -1.970197000000 -4.966958000000

---

**H<sub>2</sub>N...O<sub>2</sub> transition state (CVT)****0 2**

N	-0.923419000000	0.041417000000	-4.466006000000
H	-1.850239000000	0.257158000000	-4.076317000000
H	-1.020819000000	0.311495000000	-5.453412000000
O	-0.873637000000	-2.807575000000	-4.544351000000
O	-1.609222000000	-1.931919000000	-4.956857000000

---

**NH<sub>2</sub>O<sub>2</sub>****0 2**

N	-0.993500000000	-0.246769000000	-4.585410000000
H	-1.275440000000	0.253034000000	-5.432116000000
H	0.016397000000	-0.385389000000	-4.669478000000
O	-1.086639000000	-2.101407000000	-5.947771000000
O	-1.520311000000	-1.591967000000	-4.818951000000

---

**NH<sub>2</sub>O<sub>2</sub> to HNOOH isomerization transition state****0 2**

N	-0.866164000000	-0.322962000000	-4.766088000000
H	-1.022005000000	-0.417966000000	-5.999641000000
H	-0.121827000000	-0.311163000000	-4.061561000000
O	-1.629000000000	-1.556968000000	-6.247618000000
O	-1.402344000000	-1.566113000000	-4.841573000000

---

**HNOOH****0 2**

N	-0.938588000000	-0.400379000000	-4.338147000000
H	-1.587555000000	-1.848347000000	-6.731016000000
H	-0.042251000000	-0.400192000000	-4.845041000000
O	-0.934970000000	-2.012630000000	-6.030945000000
O	-1.671138000000	-1.354727000000	-4.886722000000

---

**HNO...OH transition state****0 2**

N	-0.988597000000	-0.308621000000	-4.417805000000
H	-1.677776000000	-1.915889000000	-6.749208000000
H	0.012292000000	-0.416464000000	-4.676966000000
O	-0.899064000000	-2.020940000000	-6.177367000000
O	-1.621357000000	-1.354361000000	-4.810526000000

---

**HNO...OH complex****0 2**

N	-1.021791000000	-0.376321000000	-4.313925000000
H	-0.004683000000	-2.364034000000	-5.712997000000
H	0.022493000000	-0.507140000000	-4.381934000000
O	0.974443000000	-2.424901000000	-5.733018000000
O	-1.550032000000	-1.266033000000	-4.963602000000

---

**HONHO****0 2**

N	-0.618693000000	-0.705993000000	-4.978775000000
H	0.189225000000	-1.340627000000	-6.548323000000
H	-0.320271000000	-0.579130000000	-4.008288000000
O	0.567759000000	-0.995584000000	-5.722940000000
O	-1.652581000000	-1.350201000000	-5.233897000000

---

**HO...HNO transition state****0 2**

N	-0.958261000000	-0.517906000000	-4.859628000000
H	0.388228000000	-1.570759000000	-6.265378000000
H	0.012898000000	-0.884154000000	-4.477301000000
O	0.624384000000	-0.760680000000	-5.782687000000
O	-1.833862000000	-1.262478000000	-5.186220000000

---

**HNO****0 1**

O	-0.495733000000	0.574201000000	-1.114421000000
N	0.314045000000	0.587008000000	-2.020841000000
H	0.892110000000	-0.298577000000	-1.956701000000

---

**NO****0 2**

N	-1.459474000000	0.000000000000	-4.336274000000
O	-1.448848000000	0.000000000000	-3.178051000000

---

**H<sub>2</sub>O****0 1**

O	-2.187285000000	-2.975650000000	0.406536000000
H	-2.187285000000	-2.220346000000	1.013630000000
H	-2.187285000000	-3.730955000000	1.013629000000

---

**OH****0 2**

O	-2.187285000000	-2.968181000000	0.417600000000
H	-2.187285000000	-3.743509000000	1.010955000000

---

**NH<sub>2</sub>O****0 2**

N	-0.480944000000	0.230307000000	0.860849000000
H	-0.823816000000	-0.724918000000	0.859488000000
H	0.228862000000	0.510171000000	1.530100000000
O	-0.940716000000	1.075385000000	0.026366000000

---

<b>CH<sub>3</sub></b>			
<b>0 2</b>			
C	0.071449000000	-0.158350000000	-0.053378000000
H	-0.324249000000	-0.116213000000	-1.059685000000
H	-0.561526000000	-0.478225000000	0.763950000000
H	1.100137000000	0.119351000000	0.135565000000

---

<b>CH<sub>3</sub> + O<sub>2</sub></b>			
<b>0 2</b>			
O	-6.908124000000	13.218026000000	6.242675000000
O	-7.051549000000	12.866473000000	5.090765000000
C	6.602427000000	-11.998571000000	-4.671332000000
H	6.156473000000	-11.824455000000	-5.634241000000
H	6.084809000000	-12.591165000000	-3.938345000000
H	7.566035000000	-11.580197000000	-4.441556000000

---

<b>CH<sub>3</sub> ··· O<sub>2</sub> transition state (CVT)</b>			
<b>0 2</b>			
O	-0.556449000000	1.766243000000	1.985397000000
O	-0.814951000000	1.617708000000	0.803421000000
C	0.173143000000	-0.358711000000	-0.213766000000
H	-0.257780000000	-0.223443000000	-1.190317000000
H	-0.303343000000	-1.019793000000	0.488621000000
H	1.176027000000	-0.017939000000	-0.025326000000

---

<b>CH<sub>3</sub>O<sub>2</sub></b>			
<b>0 2</b>			
O	-0.370238000000	1.402233000000	1.743128000000
O	-0.661174000000	1.199622000000	0.465159000000
C	0.001904000000	-0.004795000000	-0.002896000000
H	-0.280009000000	-0.109969000000	-1.045977000000
H	-0.348247000000	-0.846929000000	0.585514000000
H	1.074411000000	0.123902000000	0.103101000000

---

## References

- (1) Bao, J. L.; Truhlar, D. G. Variational Transition State Theory: Theoretical Framework and Recent Developments. *Chem. Soc. Rev.* **2017**, *46*, 7548–7596.
- (2) Grimme, S. Supramolecular Binding Thermodynamics by Dispersion-Corrected Density Functional Theory. *Chem. - Eur. J.* **2012**, *18*, 9955–9964.
- (3) Wilson, E. B.; Decius, J. C.; Cross, P. C. *Molecular Vibrations: The Theory of Infrared and Raman Vibrational Spectra*; Courier Corporation, 1980.
- (4) Jackels, C. F.; Gu, Z.; Truhlar, D. G. Reaction-Path Potential and Vibrational Frequencies in Terms of Curvilinear Internal Coordinates. *J. Chem. Phys.* **1995**, *102*, 3188–3201.
- (5) Bakken, V.; Helgaker, T. The Efficient Optimization of Molecular Geometries Using Redundant Internal Coordinates. *J. Chem. Phys.* **2002**, *117*, 9160–9174.
- (6) Ellingson, B. A.; Lynch, V. A.; Mielke, S. L.; Truhlar, D. G. Statistical Thermodynamics of Bond Torsional Modes: Tests of Separable, Almost-Separable, and Improved Pitzer–Gwinn Approximations. *J. Chem. Phys.* **2006**, *125*, 084305.
- (7) East, A. L.; Radom, L. Ab Initio Statistical Thermodynamical Models for the Computation of Third-Law Entropies. *J. Chem. Phys.* **1997**, *106*, 6655–6674.
- (8) Halkiadakis, E. A.; Bowrey, R. G. The Estimation of Molecular Parameters for the Stockmayer (12-6-3) Potential Using Critical Properties. *Chem. Eng. Sci.* **1975**, *30*, 53–60.
- (9) Joback, K. G.; Reid, R. C. Estimation of Pure-Component Properties From Group-Contributions. *Chem. Eng. Commun.* **1987**, *57*, 233–243.

- (10) Atkinson, R.; Baulch, D. L.; Cox, R. A.; Crowley, J. N.; Hampson, R. F.; Hynes, R. G.; Jenkin, M. E.; Rossi, M. J.; Troe, J.; IUPAC Subcommittee Evaluated Kinetic and Photochemical Data for Atmospheric Chemistry: Volume II - Gas Phase Reactions of Organic Species. *Atmos. Chem. Phys.* **2006**, *6*, 3625–4055.
- (11) Lente, G.; Ósz, K. Barometric Formulas: Various Derivations and Comparisons to Environmentally Relevant Observations. *ChemTexts* **2020**, *6*, 1–14.
- (12) Atmospheric Administration and United States Committee on Extension to the Standard Atmosphere *US Standard Atmosphere, 1976*; National Oceanic and Atmospheric Administration, 1976.
- (13) Andersson, K.; Malmqvist, P. A.; Roos, B. O.; Sadlej, A. J.; Wolinski, K. Second-order Perturbation Theory With a CASSCF Reference Function. *J. Phys. Chem.* **1990**, *94*, 5483–5488.
- (14) Ghigo, G.; Roos, B. O.; Malmqvist, P.-Å. A Modified Definition of the Zeroth-order Hamiltonian in Multiconfigurational Perturbation Theory (CASPT2). *Chem. Phys. Lett.* **2004**, *396*, 142–149.
- (15) Dyal, K. G. The Choice of a Zeroth-order Hamiltonian for Second-order Perturbation Theory With a Complete Active Space Self-consistent-field Reference Function. *J. Chem. Phys.* **1995**, *102*, 4909–4918.
- (16) Koopmans, T. Über die Zuordnung von Wellenfunktionen und Eigenwerten zu den Einzelnen Elektronen Eines Atoms. *Physica* **1934**, *1*, 104–113.
- (17) Andersson, K.; Roos, B. O. Multiconfigurational Second-order Perturbation Theory: A Test of Geometries and Binding Energies. *Int. J. Quantum Chem.* **1993**, *45*, 591–607.
- (18) Salo, V.-T.; Chen, J.; Runeberg, N.; Kjaergaard, H. G.; Kurtén, T. Multireference and

Coupled-Cluster Study of Dimethyltetraoxide (MeO<sub>4</sub>Me) Formation and Decomposition. *J. Phys. Chem. A* **2024**, *128*, 1825–1836.

(19) Ruscic, B.; Pinzon, R. E.; Morton, M. L.; von Laszewski, G.; Bittner, S. J.; Nijssure, S. G.; Amin, K. A.; Minkoff, M.; Wagner, A. F. Introduction to Active Thermochemical Tables: Several “Key” Enthalpies of Formation Revisited. *J. Chem. Phys. A* **2004**, *108*, 9979–9997.

(20) Ruscic, B.; Bross, D. Active Thermochemical Tables (ATcT) Values Based on ver. 1.202 of the Thermochemical Network (2024).